Nonplanar sensing skins for structural health monitoring based on electrical resistance tomography

Jauhiainen, Jyrki

2021-12

Jauhiainen , J , Pour-Ghaz , M , Valkonen , T & Seppänen , A 2021 , ' Nonplanar sensing skins for structural health monitoring based on electrical resistance tomography ' , Computer-Aided Civil and Infrastructure Engineering , vol. 36 , no. 12 , pp. 1488-1507 . https://doi.org/10.1111/mice.

http://hdl.handle.net/10138/336638
https://doi.org/10.1111/mice.12689

DOI: 10.1111/mice.12689

RESEARCH ARTICLE

COMPUTER-AIDED CIVIL AND INFRASTRUCTURE ENGINEERING WILEY

Nonplanar sensing skins for structural health monitoring based on electrical resistance tomography

Jyrki Jauhiainen[1] | **Mohammad Pour-Ghaz**[2] | **Tuomo Valkonen**[3,4] | **Aku Seppänen**[1]

[1] Department of Applied Physics, University of Eastern Finland, Kuopio, Finland

[2] Department of Civil Construction and Environmental Engineering, North Carolina State University, Raleigh, NC, USA

[3] ModeMat, Escuela Politécnica Nacional, Quito, Ecuador

[4] Department of Mathematics and Statistics, University of Helsinki, Helsinki, Finland

Correspondence
Aku Seppänen, University of Eastern Finland, Department of Applied Physics, Kuopio Campus, P.O. Box 1627, FI-70211, Kuopio, Finland.
Email: aku.seppanen@uef.fi

Funding information
European Union's Horizon 2020 research and innovation programme, Grant/Award Number: 764810; Academy of Finland (Centre of Excellence of Inverse Modelling and Imaging, 2018-2025, Grant/Award Number: 303801; European Union's Horizon 2020 research and innovation programme, Grant/Award Number: 764810; Academy of Finland Centre of Excellence of Inverse Modelling and Imaging, 2018-2025, Grant/Award Number: 303801; Academy of Finland, Grant/Award Numbers: 314701, 320022

Abstract

Electrical resistance tomography (ERT)-based distributed surface sensing systems, or sensing skins, offer alternative sensing techniques for structural health monitoring, providing capabilities for distributed sensing of, for example, damage, strain, and temperature. Currently, however, the computational techniques utilized for sensing skins are limited to planar surfaces. In this paper, to overcome this limitation, we generalize the ERT-based surface sensing to nonplanar surfaces covering arbitrarily shaped three-dimensional structures; we construct a framework in which we reformulate the image reconstruction problem of ERT using techniques of Riemannian geometry, and solve the resulting problem numerically. We test this framework in series of numerical and experimental studies. The results demonstrate the feasibility of the proposed formulation and the applicability of ERT-based sensing skins to nonplanar geometries.

1 | INTRODUCTION

A component of structural health monitoring (SHM) is a sensor network consisting of variety of sensors utilizing a variety of techniques that continuously monitor the condition of the infrastructure (Worden & Dulieu-Barton, 2004). Some of these techniques focus on monitoring global properties of the structure (Z. Li et al., 2017; Oh et al., 2017; Ozdagli & Koutsoukos, 2019; Perez-Ramirez et al., 2019; Rafiei & Adeli, 2017), while other techniques focus on localized damage detection (Hampshire & Adeli, 2000).

One important aim of SHM is the automatic detection of cracks in concrete structures. For example, crack detection from photographs of concrete structures has undergone significant developments in recent years (Deng et al., 2020; S. Li et al., 2019; Nayyeri et al., 2019; Ni et al., 2019; X. Zhang, Rajan et al., 2019). Some of this research focused on specific applications, such as monitoring bridges (Y.-F. Liu, Nie et al., 2020; C. Zhang et al., 2020) or road pavements (Bang et al., 2019; J. Liu, Yang et al., 2020; Ni et al., 2019; Rodriguez-Lozano et al., 2020; A. Zhang, Wang et al., 2019).

While the sensing techniques have advanced significantly over the past 20 years, utilization of SHM to real-life infrastructure is still relatively rare. Many factors contribute to the slow adaptation of SHM for infrastructure, including the high cost of implementing and maintaining, as well as difficulty in the interpretation of measurements. For a review on interpretation of nonlinear measurements, see Amezquita-Sanchez and Adeli (2019). The interpretation of the measurements is especially challenging when a large number of discrete sensors are used without the utilization of a model-based interpretation approach. Distributed sensors and sensing systems may offer an alternative that at times can be more cost effective. Especially, distributed sensors that are model based and provide direct visualization of the data can overcome many of the limitations of discrete sensors. An example of such a system is an electrical resistance tomography (ERT)-based sensing skin (Hallaji & Pour-Ghaz, 2014).

ERT-based sensing skin is a distributed surface sensing system that uses a layer of electrically conductive material—such as colloidal metallic paint (Hallaji & Pour-Ghaz, 2014; Hallaji et al., 2014) or carbon nanotube film (Loh et al., 2007, 2009)—which is applied to a surface of a structure. Also, a set of electrodes is placed on the surface, and based on multiple electric current/potential excitations and measurements from the electrodes, the spatially distributed electrical conductivity of the sensing layer is reconstructed. The surface coating material is designed so that the changes in its electrical conductivity give information on physical or chemical conditions of the underlying structure.

One application of the ERT-based sensing skins is damage detection (Hallaji & Pour-Ghaz, 2014; Hallaji et al., 2014; Loh et al., 2007, 2009). Cracking of the structure surface breaks also the sensor layer, decreasing the conductivity of the layer material locally. The ERT reconstruction that represents the electrical conductivity of the layer thus reveals the crack pattern on the surface. ERT-based sensing skins have also been developed for detection of pressure changes (Chossat et al., 2015), strains (Loh et al., 2009; Tallman et al., 2014), pH changes (Hou et al., 2007), chloride ions (Seppänen et al., 2017), and temperature distributions (Rashetnia et al., 2017). We note that for strain imaging, a different type of sensing skin based on electrical capacitance measurements has also been recently introduced (Downey et al., 2016; Laflamme et al., 2016).

One of the potential advantages of the sensing skin technique in SHM is its excellent scalability: ERT has been used for imaging objects with spatial dimensions ranging from millimeters (Wu et al., 2018) to kilometers (He et al., 2020). Thus far, the largest sensing skin has been of size 4 m^2 (Rashetnia et al., 2018).

In the above cited papers, ERT-based sensing skins were applied to planar geometry only. In many applications, however, the structures of interest have a complex three-dimensional (3D) geometry, and the surface to be monitored is nonplanar; examples of such target structures are pipelines, pumps, and pressure vessels.

In addition to SHM, ERT-based sensing systems have been applied to robotics, where the sensing skin is used for detecting and localizing touch via pressure sensing (Alirezaei et al., 2007, 2009; Yousef et al., 2011). In a publication (Silvera Tawil et al., 2012), an ERT-based touch sensor made of conductive fabric was wound around an artificial arm. The winding did not cause wrinkles to the fabric, but since the fabric was bent, the geometry was nonplanar. The computational model used in the study, however, assumed a planar geometry. Although earlier studies have indicated that at least certain sensing skin materials are very sensitive to stretching and bending (Alirezaei et al., 2007, 2009), neglecting these effects by the use of planar approximation did not cause significant reconstruction artifacts in the study of Silvera Tawil et al. (2012). Nevertheless, it is not guaranteed that the planar approximation works with all materials, especially when aiming at imaging the electrical conductivity quantitatively (Hallaji et al., 2014). Even more importantly, in many potential SHM applications, the planar approximation of the sensor is impossible, because of the nontrivial topology of the surface. This is the case, for example, with all the geometries considered in the numerical and experimental studies of this paper (Figure 1).

Another application, very similar to SHM with sensing skin, is the use of ERT with self-sensing materials (Tallman et al., 2014, 2015). Recently, ERT was used for damage detection on a nonplanar structure using a sensor made of self-sensing composite tubes (Thomas et al., 2019). In this case, the 3D structure of the target material was modeled as in other 3D ERT applications (Brown, 2003; Loke & Barker, 1996; Vauhkonen, 2004). While in self-sensing applications, the structures—and thus also sensors—are inherently 3D, in sensing skin applications, the thickness of a sensor is several orders of magnitudes lower than its other dimensions. Clearly, this type of sensor can be modeled as a surface in 3D space, and a full

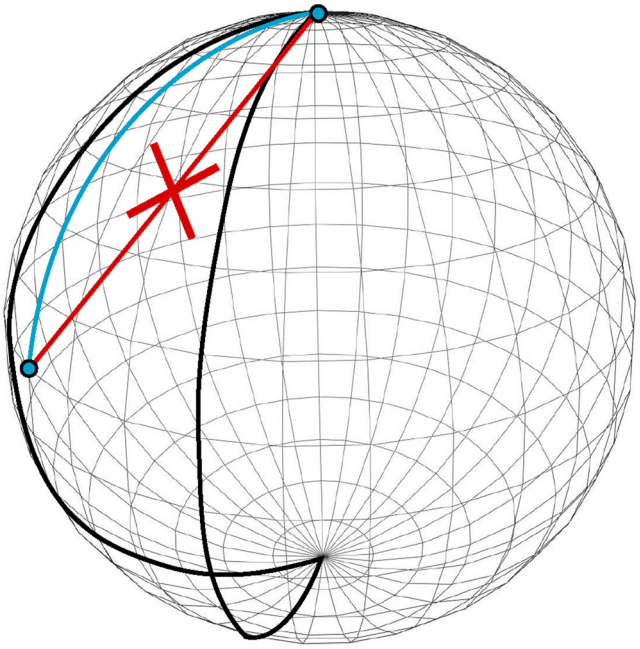

FIGURE 1 An illustration of how the shortest path between two points in the nonplanar 2D model differs from the shortest path between these points in the 3D model. Essentially the Riemannian metric determines how the distance is defined in the domain

3D model would be unnecessarily complicated, making the computations more complex and more prone to numerical errors.

In this paper, we formulate the problem of imaging a thin, electrically conductive surface material—sensing skin—applied on an arbitrarily shaped 3D object by modeling it as a 2D surface in the 3D space, or, mathematically as a two-manifold. The mathematical treatment of this formulation is shown in the Appendix. The main focus of this paper is the numerical and experimental evaluation of this approach. We study the approach in three nonplanar geometries. In these studies, we consider two target applications: crack detection and imaging of diffusive processes (such as heat conduction on solid materials).

2 | NONPLANAR ERT IMAGING

In ERT imaging, the conductivity of the target is reconstructed from the voltage and current data obtained through a set of electrodes placed on the surface of the target. Typically, the target is treated as a 3D or as a planar 2D domain. However, in order to reconstruct the conductivity of an arbitrary shaped sensing skin, we consider the target as an arbitrary surface in three dimensions.

In this section, we first introduce a model that describes the ERT measurements given the surface conductivity; this is referred to as the *forward model* of ERT, and it is approximated numerically using the finite element method (FEM). The *inverse problem* of ERT is to reconstruct the conductivity given the current/potential measurements. The inverse problem is ill-posed in the sense that the "conventional" solutions to this problem are nonunique and extremely intolerant to measurement noise and modeling errors. For this reason, the solutions of the inverse problem require a priori information on the conductivity, or *regularization* of the problem (Kaipio & Somersalo, 2006). In this paper, we formulate the inverse problem as a regularized least squares problem, where the data fidelity term utilizes the FEM approximation of the forward model.

2.1 | Modeling of measurements

Consider a measurement setup in which the measurement data are obtained by sequentially setting each electrode to a known potential, grounding others, and measuring the electric current caused by potential difference through all of the grounded electrodes. Given L electrodes, this amounts to $L-1$ current measurements for each excitation and $L \times (L-1)$ measurements in total. We note that many of the existing ERT measurement systems operate the other way round—using current excitations and potential measurements. However, for such a system, the formulation of both the forward and inverse problem are analogous with the formulation written in this section. The choice of using potential excitations and current measurements is made because the commercial measurement device employed for the experiments (Section 4) uses this procedure.

The measurement setting described above constitutes the following forward problem: solve the electric current $I_k^p(\sigma)$ through each electrode k, given the spatially distributed conductivity $\sigma(x)$ (where $x = (x_1, x_2, x_3)$ is the spatial variable) and a set of electric potentials U_k^p corresponding to an excitation $p = 1, 2, \ldots, L$. We model this relation using the complete electrode model (CEM) (Cheng et al., 1989), which consists of a partial differential equation and a set of boundary conditions,

$$\nabla \cdot (\sigma(x) \nabla u^p(x)) = 0 \quad x \in M \tag{1a}$$

$$u^p(x) + \zeta_k \sigma \langle \nabla u^p(x), \hat{n} \rangle_g = U_k^p \quad x \in \partial M_{e_k} \tag{1b}$$

$$\int_{\partial M_{e_k}} \sigma \langle \nabla u^p(x), \hat{n} \rangle_g \, d\tilde{S} = -I_k^p \tag{1c}$$

$$\sigma \langle \nabla u^p(x), \hat{n} \rangle_g = 0 \quad x \in \partial M \setminus \bigcup_{k=1}^{L} \partial M_{e_k} \tag{1d}$$

where u^p is the inner electric potential, $M \subset \mathbb{R}^3$ is a surface with boundary ∂M, ∂M_{e_k} is the part of the ∂M representing the edge of the kth electrode, ζ_k is contact resistance, and $\langle \cdot, \cdot \rangle_g$, which we will shortly define precisely, is an inner product on the tangent vectors of the surface M, $-\hat{n}$ is an inward unit normal of ∂M (i.e., a vector tangent to M, pointing inward), and L is the number of electrodes. In addition, the currents I_k^p are required to satisfy Kirchhoff's law $\sum_{k=1}^{L} I_k^p = 0$. We write $d\tilde{S}$ for the infinitesimal length elements of the 1D boundary ∂M_{e_k}.

By calling M a surface, we mean that we can parameterize $x = (\phi^1(y^1, y^2), \phi^2(y^1, y^2), \phi^3(y^1, y^2))$ *locally* for some $(y^1, y^2) \in U \subset \mathbb{R}^2$ and some $x \in V \subset M$. This means that the functions and differential operators in (1) are 2D, and can be formally defined through Riemannian geometry.

Formally, we equip *manifold* M with a *Riemannian metric* g. The metric g defines an inner product on the tangent planes of M. Specifically, for tangent vectors v, w, we take $\langle v, w \rangle_g := g(v, w)$, which can be locally computed by $g(v, w) = \sum_{i=1}^{2} \sum_{j=1}^{2} g_{ij} v^i w^j$. In practice M is an embedded manifold and we define g as the *pullback* of the standard dot product in $\mathbb{R}^3$ to M, so that g induces the geodesic distance on M, as illustrated in Figure 1. Furthermore, g defines the divergence and the gradient operators on M;

$$\nabla \cdot f = \frac{1}{\sqrt{|g|}} \sum_{i=1}^{2} \partial_i \left(\sqrt{|g|} f^i \right) \text{ and } \nabla \hat{f} = \sum_{i=1}^{2} \sum_{j=1}^{2} g^{ij} \partial_j \hat{f} \partial_i \tag{2}$$

where $f : M \to \mathbb{R}^2$ (e.g., $f = \sigma \nabla u^p$), $\hat{f} : M \to \mathbb{R}$ (e.g., $\hat{f} = u^p$). The maps ∂_i generalize directional derivatives to M; technically $\partial_i : F(M) \to F(M)$, where $F(M)$ is a collection of differentiable functions on M and $i = 1, 2$, form a local basis for the tangent plane. On this basis, g_{ij} are the components of matrix that represent g, g^{ij} are the components of the inverse of this matrix, and $|g|$ is the determinant of this matrix. Furthermore, $d\tilde{S}$ in (1) is the Riemannian volume measure of a curve (length in $\mathbb{R}^3$) in $(\partial M, g_\omega)$, where g_ω is the pullback of g to ∂M.

Finally, we note that since the conductivity σ is distributed on the surface M, which is locally 2D, it represents a 2D (surface) conductivity instead of volumetric conductivity considered in 3D ERT. As in the planar sensing skin cases (Hallaji et al., 2014), this model is a natural choice, because the thickness of the imaged paint layer is several orders of magnitude smaller than its other dimensions.

2.2 | Variational form and numerical approximation of the forward model

We approximate (1) with a Galerkin FEM, as described in detail in the Appendix. Indeed, by introducing test function (v, V), we can write (1) in a variational form

$$\begin{aligned} &\int_M \sigma \langle \nabla v, \nabla u^p \rangle_g dS + \sum_k^L \frac{1}{\zeta_k} \int_{\partial M_{e_k}} (u^p v - u^p V_k) d\tilde{S} \\ &\quad - \sum_k^L \int_{\partial M_{e_k}} \sigma \langle \nabla u^p(x), \hat{n} \rangle_g V_k d\tilde{S} \\ &= \sum_k^L \frac{1}{\zeta_k} \int_{\partial M_{e_k}} U_k (v - V_k) d\tilde{S} \end{aligned} \tag{3}$$

We write dS for the infinitesimal area elements of the 2D surface M. Notation wise, the variational form (3) is almost the same as the one written for the 3D ERT (Voss, 2020). However, the functions in (3) are defined on only the surface $M \subset \mathbb{R}^3$, the differential operators are defined according to (2), and inner product is defined with respect to the Riemannian metric g.

Furthermore, by approximating $u^p = \sum_j^N u_j^p v_j$ and $I_k^p = (\sum_j^{L-1} \check{I}_j n_j)_k$, where v_j is piecewise linear and $n_j \in R^L$, such that the first component of n_j is always 1 and the $j+1$ component is -1 and other indices are zero, (3) admits the matrix form

$$\begin{bmatrix} D_1 & 0 \\ D_2 & D_3 \end{bmatrix} \begin{bmatrix} \bar{u} \\ \bar{I} \end{bmatrix} = \begin{bmatrix} \check{U}_1 \\ \check{U}_2 \end{bmatrix} \tag{4}$$

where the matrices

$$(D_1)_{i,j} = \int_M \sigma \langle \nabla v_i, \nabla v_j \rangle_g dS + \sum_k^L \frac{1}{\zeta_k} \int_{\partial M_{e_k}} v_j v_i d\tilde{S},$$

$$(D_2)_{i,j} = \frac{1}{\zeta_{i+1}} \int_{\partial M_{e_{i+1}}} v_j d\tilde{S} - \frac{1}{\zeta_1} \int_{\partial M_{e_1}} v_j d\tilde{S},$$

$$(D_3)_{i,j} = \begin{cases} 2, & i = j \\ 1, & \text{otherwise} \end{cases}$$

and the vectors $(\bar{u})_i = u_i^p, (\check{U}_1)_i = \sum_k^L \frac{U_k}{\zeta_k} \int_{\partial M_{e_k}} v_i d\tilde{S}, (\bar{I})_i = \check{I}_i$, and $(\check{U}_2)_i = -\sum_k^L \frac{1}{\zeta_k} \int_{\partial M_{e_k}} U_k (n_i)_k d\tilde{S}$.

2.3 | Inverse imaging problem

We can now concatenate the simulated measurements to form a vector $I(\sigma) = (I_1^1(\sigma), \dots, I_{L-1}^L(\sigma))^T$. Further, we denote the vector containing the corresponding measured data by I^M.

The typical approach to solve the inverse problem of ERT is to solve a conductivity that minimizes the sum of a so-called *data term*, $\frac{1}{2}\mathcal{L}(I(\sigma) - I^M)^2$, and a *regularization functional* $F(\sigma)$. The norm of the data term is L_2 norm, due to the assumption of Gausssian distributed noise, while the regularization may contain nonsmooth terms, such as L_1 norms.

In sensing skin applications, however, we may improve the reconstruction quality by utilizing measurements I_{ref}^M, measured from an initial stage where the sensing skin is intact (Hallaji et al., 2014), to compute a homogeneous estimate σ_{ref} for the initial (background) conductivity of the sensing skin;

$$\sigma_{\text{ref}} := \arg\min_{\sigma \in \mathbb{R}^+} \frac{1}{2}\|I(\sigma) - I_{\text{ref}}^M\|^2 \tag{5}$$

Based on this estimate, we compute a discrepancy term $\epsilon := I_{\text{ref}}^M - I(\sigma_{\text{ref}})$, which gives an approximation of the modeling error caused by neglecting the inhomogeneity of the background conductivity of the sensing skin. To compensate for this modeling error in the reconstruction of the conductivity σ in the *subsequent* stages, we add this term into the model $I(\sigma)$ (Hallaji et al., 2014), and reconstruct the conductivity σ as a solution of a minimization problem

$$\hat{\sigma} := \arg\min_{\sigma \in V} \frac{1}{2}\|\mathcal{L}(I(\sigma) - I^M + \epsilon)\|^2 + F(\sigma) \tag{6}$$

where $V = \{f(x) \in H_N(M) \mid \sigma_{\min} \le f(x) \le \sigma_{\max}, x \in M\}$, $H_N(M)$ is a finite dimensional function space on M, and $\mathcal{L}$ is a matrix for which $\mathcal{L}^T\mathcal{L}$ is so-called *data precision matrix*, that is, the inverse of the noise covariance matrix. Furthermore, the lower constraint $\sigma_{\min} > 0$ comes from the natural, physics-based limit for the positivity of the conductivity and the upper constraint $\sigma_{\max}$ restricts the conductivity from above whenever the maximum conductivity is known. In cases where the maximum conductivity is unknown, we set $\sigma_{\max}$ to an arbitrary large number.

The regularization function $F(\sigma)$ in (6) is chosen depending on the information that is available about the conductivity prior to the measurements. In the numerical and experimental cases of the following sections, we consider two choices of regularization functionals (7) and (8). We note, however, that the nonplanar ERT scheme proposed in this paper is not restricted to any particular choices of regularization. Although the above modeling error correction method based on the discrepancy term ϵ is highly approximative, it has been shown to be useful in several cases, especially when the background conductivity is inhomogeneous (Hallaji et al., 2014), and is thus used also in this paper. A more advanced formulation of the inverse problem for detecting complex crack patterns in the presence of inhomogeneous background was proposed in Smyl et al. (2018). If needed, this computational method would also be directly applicable to the nonplanar ERT model described above.

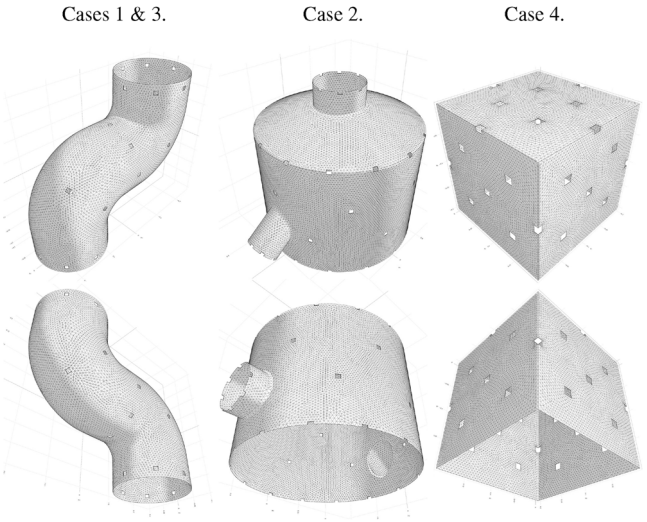

FIGURE 2 Geometries of the sensing skins used in the numerical simulation studies (left and middle columns) and in experimental study (right column). The surface triangulations correspond to the finite element meshes used in the respective image reconstructions. The square-shaped nontriangulated patches of the surface represent the electrodes for the electrical measurements

3 | NUMERICAL SIMULATION STUDIES

We evaluate the proposed ERT imaging scheme with numerical simulation studies using two nonplanar geometries; one resembles a pipe segment (first column in Figure 2) and one resembles a pressure vessel (second column in Figure 2). These geometries represent a thin conductive layer, a sensing skin, on a solid object or the surface of this object itself. This object, however, is not necessarily hollow.

Figure 2 also illustrates the locations of the electrodes. We note that majority of them are *internal electrodes*, in the sense that they are surrounded by the sensing skin. These electrodes are modeled by creating holes on the surface, and the boundaries of these holes are treated as electrodes. Indeed, the mathematical formulation does not distinguish between the internal or the "typical" electrodes

(or "internal" and "external" border for that matter) as they are both simply located on the boundary of the domain. The use of internal electrodes improves the quality of ERT reconstructions from the case where all electrodes are in the perimeter of the sensing skin even in planar geometries (Rashetnia et al., 2018)—in nonplanar imaging, the effect is presumably even stronger.

Generally, the sensitivity of ERT measurements decreases as a function of distance from the (nearest) electrodes. For this reason, we attempted to place the electrodes evenly, so that the sensitivity would be somewhat uniform. In this paper, we did not explore the problem of optimal experimental design in ERT systematically, but we note that the optimal placement sensors and other related devices (Gutierrez Soto & Adeli, 2013) are topics of great importance in engineering. In ERT, most of this research has focused on optimizing the current injections. For current pattern optimization in deterministic and Bayesian frameworks, respectively, we refer to Isaacson (1986) and Kaipio et al. (2004). The optimal electrode positioning in ERT has been studied in Hyvonen et al. (2014). In the context of sensing skins, the effect of internal electrodes to the sensitivity of measurements has been addressed in Rashetnia (2017).

In this section, we consider two target applications: crack detection and imaging of diffusive processes (such as distributed temperature sensing; Rashetnia et al., 2017).

Both geometries are used to study crack detection (Cases 1 and 2). In each geometry, we consider five stages of cracking. In the first stage, stage 0, the sensing skin is intact and the conductivity is homogeneous. Measurements simulated in this stage are used as the reference measurements I^M_{ref} and utilized for computing the homogeneous background estimate (5). In the subsequent stages, to simulate evolving crack pattern, we lower the conductivity at the locations that correspond to the cracks. The diffusive process imaging is studied in Case 3, where the geometry is same as in Case 1. Here, the conductivity distribution is spatially smooth, and it evolves in the diffusive manner, mimicking an application where the surface temperature distribution is monitored using a sensing skin.

3.1 | Specification of geometries and simulation of data

The first column in Figure 2 shows the pipe segment geometry. The radius of the pipe segment is 0.100 m and it consists of three 0.100-m-long straight cylindrical sections connected by two curved sections that both turn 90 degrees to form an "S"-shaped geometry. The three straight sections each have eight symmetrically placed electrodes on them and the two curved sections both have four electrodes on their convex side. These electrodes are square shaped with 0.010 m side length.

The second column in Figure 2 shows the geometry of a pressure vessel. The diameter of the pressure vessel is 1 m and the length of the cylindrical middle section is 1.500 m. The radius of curvature for the spherical top section is 2.125 m. Furthermore, the chamber has three cylindrical extensions. One of the extensions is attached to the top section of the chamber. The radius of this extension is 0.300 m. The other two extensions are attached on the cylindrical section. The radius of the larger horizontal extension is 0.250 m and the radius of the smaller diagonal extension is 0.200 m. On each extension, eight electrodes are placed radially. Furthermore, the cylindrical section of the chamber has four layers of radially placed electrodes. The topmost and bottommost layers have 14 electrodes each, and the two layers in between have seven and six electrodes. The total number of electrodes is 65. The inner electrodes on the main chamber are square shaped with side length of 0.050 m. The rest of the electrodes are rectangular with side lengths of 0.050 m and 0.025 m.

The FE mesh that we use in the data simulation for the pipe segment geometry has 92,578 nodes and 184,057 elements, and the FE mesh for the pressure vessel has 491,679 nodes and 980,160 elements. In each case, we initially set the surface conductivity to $\sigma(x) = 1$ S and use it to generate the reference measurements (stage 0). Subsequently, we generate measurements from four stages of varying conductivities, each stage being a continuation of the previous one (stages 1–4). In Cases 1 and 2, stages 1–4 consist of spatially narrow areas of low conductivity, $\sigma(x_{\text{crack}}) = 10^{-7}$ S (top rows in Figures 3 and 4). In Case 3, we set the minimum conductivity to 0.89 S in a single point on the curved surface, and it gradually increases to the background value of 1 S as function of space. To mimic the diffusive process, the size of the area with lowered conductivity is increased between consecutive stages from 1 to 4 (top row in Figure 5). For every simulated measurement, we set all contact resistances to $\zeta_k = 10^{-5}$ Ω, and we add Gaussian noise with a standard deviation of $10^{-4}|I^p_k|$ to each simulated current.

3.2 | Image reconstruction

We reconstruct the conductivity by solving the minimization problem of (6). In the crack detection problems in Cases 1 and 2, we utilize total variation (TV) regularization (Rudin et al., 1992)

$$F(\sigma) = TV(\sigma) \tag{7}$$

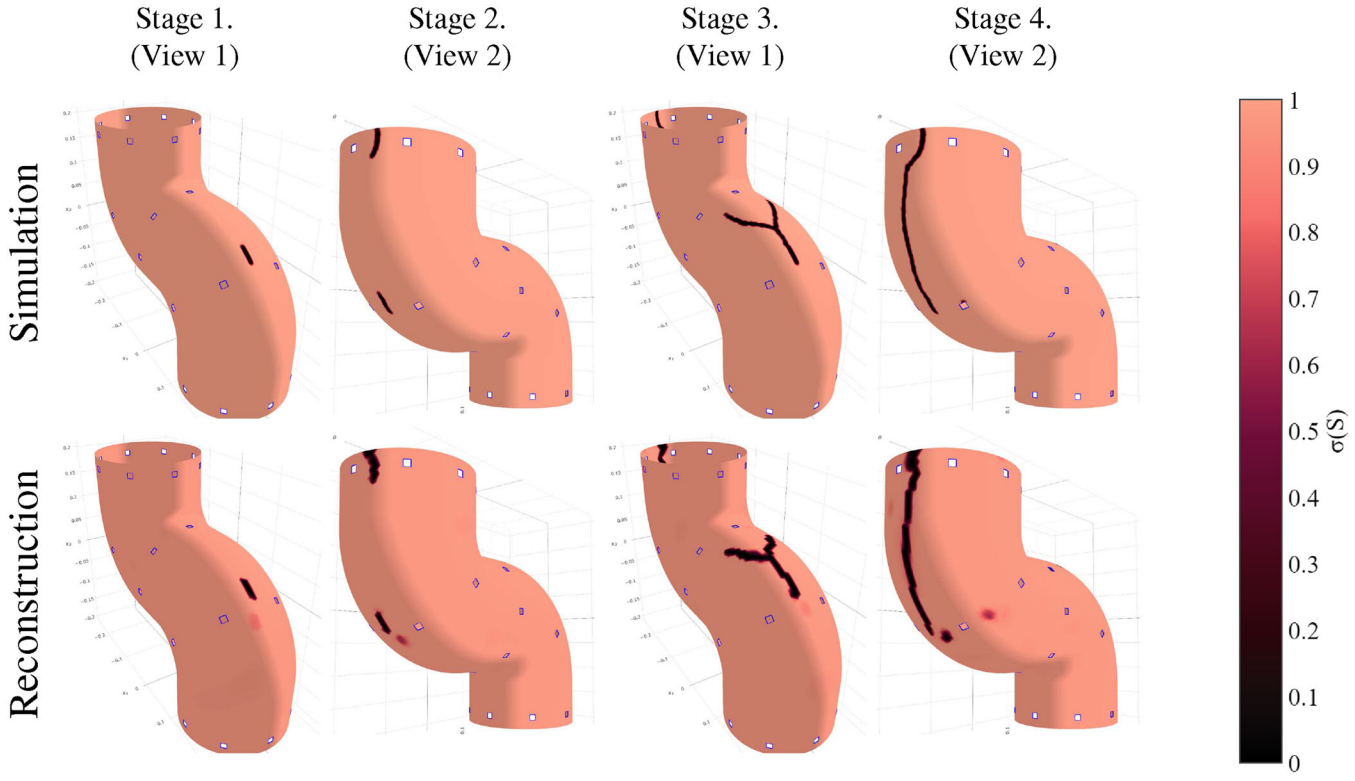

FIGURE 3 Case 1: True conductivity distribution of the sensing sensing skin (top row) and the ERT-based reconstructions of the conductivity (bottom row) corresponding to four stages of cracking. Note that the viewing angle varies between two views (View 1 and View 2) in order to show the relevant conductivity changes

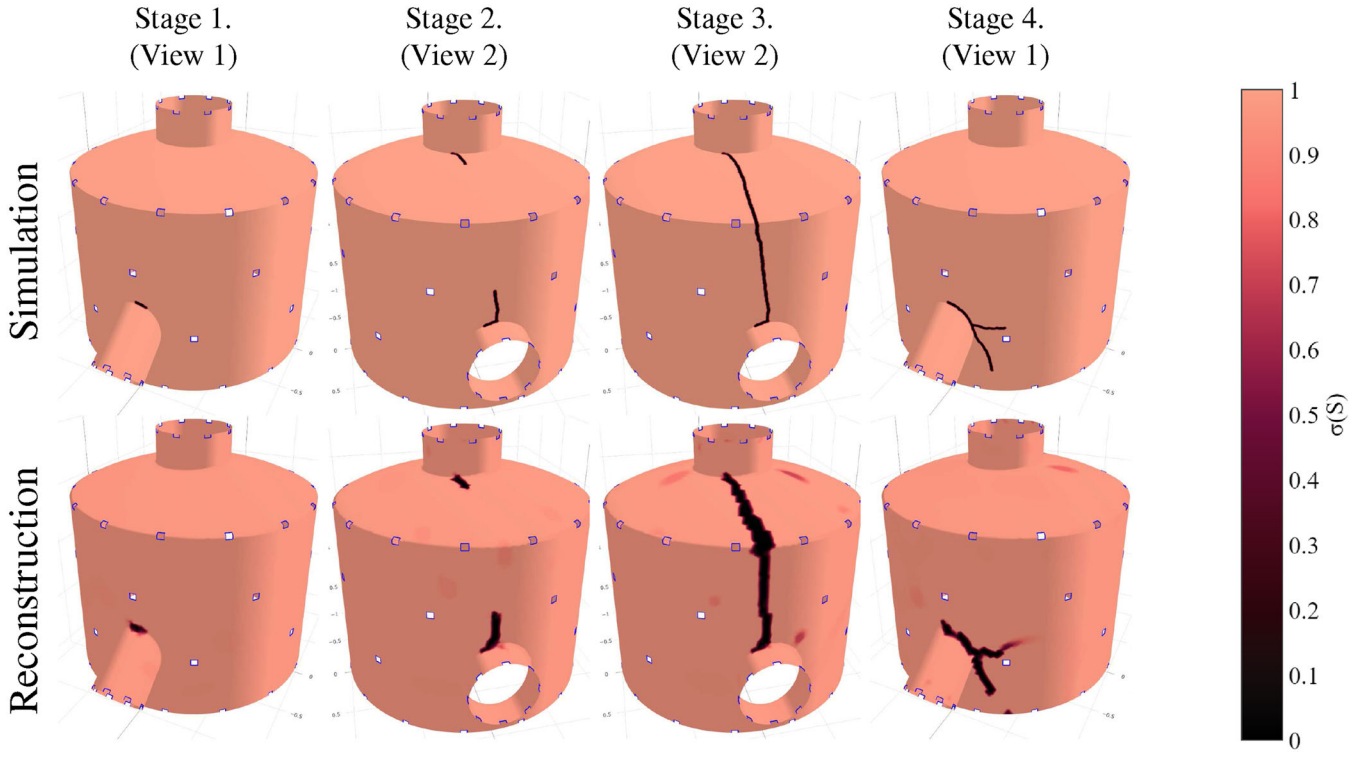

FIGURE 4 Case 2: True conductivity distribution of the sensing skin (top row) and the ERT-based reconstructions of the conductivity (bottom row) corresponding to four stages of cracking. Note that the viewing angle varies between two views (View 1 and View 2) in order to show the relevant conductivity changes

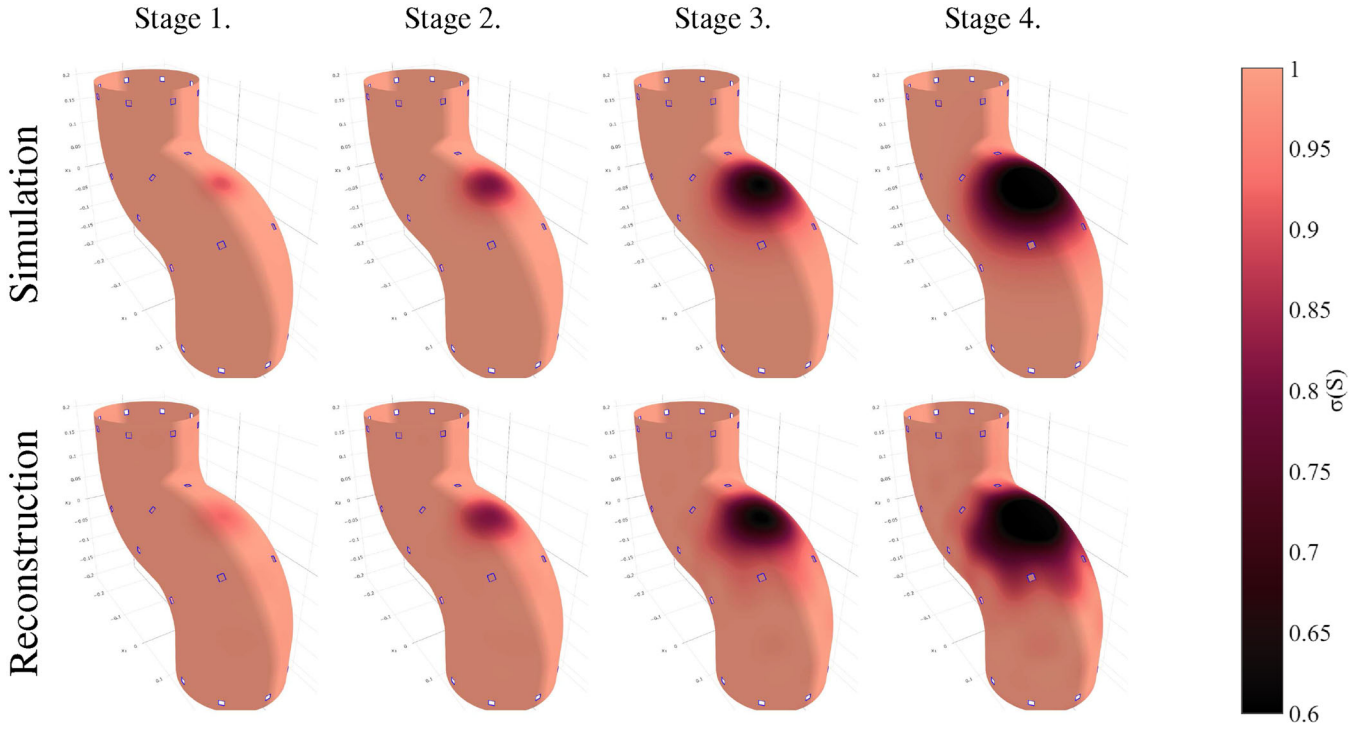

FIGURE 5 Case 3: True conductivity distribution of the sensing skin (top row) and the ERT-based reconstructions of the conductivity (bottom row) corresponding to four stages of cracking

TV regularization penalizes the magnitude of the spatial gradient of σ in L^1 norm and is often suitable for cases where the conductivity features sharp edges on a relatively homogeneous background. TV regularization is shown to be feasible in ERT-based crack detection (Hallaji et al., 2014).

In Case 3, we utilize Gaussian smoothness regularization

$$F(\sigma) = \|R_\Gamma(\sigma - \sigma_{\text{ref}})\|^2 \tag{8}$$

where R_Γ is given by $R_\Gamma = \Gamma^{-1/2}$, $\Gamma_{i,j} = ae^{-\frac{\|x^i - x^j\|^2}{2b^2}}$ (Lipponen et al., 2013), x^i, $x^j \in \mathbb{R}^3$ are the locations of the nodes i and j in the FE mesh, $a = 100$, and $b = 0.075$. This is often a feasible choice of regularization functional in cases of diffusive phenomena, because it promotes spatial smoothness of the conductivity distribution.

In all the studies, the matrix $\mathcal{L}$ is diagonal with $[\mathcal{L}]_{i,i} = 1000$ and the minimum conductivity is $\sigma_{\min} = 10^{-4}$ S. In addition, we compute a homogeneous estimate σ_{ref} using the measurements I^M_{ref} at the reference stage (stage 0). We use this estimate to compute the approximation error term $\epsilon = I^M_{\text{ref}} - I(\sigma_{\text{ref}})$ as described in Section 2.3. In Cases 1 and 2, we also use the homogeneous estimate as the maximum constraint $\sigma_{\max} = \sigma_{\text{ref}}$, which encompasses the idea that the cracks can never increase the conductivity of the conductive layer (Hallaji et al., 2014). In Case 3, we set $\sigma_{\max} = \infty$, that is, the conductivity distribution is not constrained from above. The meshes used in the image reconstruction are sparser than those used when simulating the data. For example, the mesh for the pipe segment has 10,358 nodes and 20,389 elements while the mesh for the pressure vessel mesh has 20,565 nodes and 40,532 elements.

We utilize the recently published iterative Relaxed Inexact Proximal Gauss-Newton (RIPGN) algorithm (Jauhiainen et al., 2020) to solve the minimization problem (6). RIPGN is a Gauss–Newton variant; it linearizes the nonlinear operator $I(\sigma)$ of (6) at each iterate, finds an approximate solution to the associated proximal problem using a so-called block-adapted version of primal dual proximal splitting (PDPS), and interpolates between this solution and the one computed at the previous iteration step. The PDPS algorithm was originally introduced by Chambolle and Pock (2011) and the block-adapted version was later introduced by Valkonen (2019). The RIPGN algorithm supports L_p, $p \geq 1$, functionals for the nonlinear data term and any proper, convex, and lower semicontinuous (i.e., even indicators) regularization functionals. A version of the RIPGN algorithm, specialized for this study, is described in detail in Appendix A.2.

After computing each iterate, we check the convergence of the algorithm by comparing the value of the objective

function in (6) at the current iterate to the value objective function at the previous iterates. Furthermore, we limit the maximum amount of computed iterations to 30. In the ERT problem (6), this iteration limit seems to be plenty to reach a sufficient convergence. The theoretical convergence of this algorithm is shown in Jauhiainen et al. (2020).

The reason for applying the RIPGN method to optimization in this paper is that it was shown to be very effective both in 3D and planar 2D ERT (Jauhiainen et al., 2020). We note, however, that standard Gauss–Newton and Newton methods based on smoothing the minimum and maximum constraints and the TV functional (González et al., 2017; Hallaji et al., 2014) could be utilized as well. All the code used in the study was written in Julia (1.3.1). Computations were done on AMD Ryzen 9 3950X CPU with 64 GB of RAM (DDR4, 3800 MHz, CL15). Parts of the RIPGN algorithm utilize CUDA code. CUDA code was run on Nvidia RTX 2080 Ti GPU.

3.3 | Results and discussion

3.3.1 | Case 1: Crack detection in pipeline

The results of Case 1 are illustrated in Figure 3. The top row shows the (true) simulated conductivity, and the reconstructed conductivity is depicted in the bottom row. Each column corresponds to a different cracking stage. Each reconstruction took 5 to 11 min to compute. These computation times, obviously, depend on the chosen computational approach and available computational resources. While our focus is not on optimization of the computational efficiency, we note that in previous applications of ERT, the computation times have been reduced by 2–3 orders of magnitude, by specifically developed model reduction techniques in the image reconstruction (Lipponen et al., 2013).

In the first stage (Figure 3, column 1), a crack forms at the middle section of the pipe segment. The reconstruction captures the shape of this crack quite accurately and only a small artifact is visible near the crack. The conductivity value at the crack is 10^{-4} S, which equals to $\sigma_{\min}$.

In the second stage (Figure 3, column 2), two new cracks appear in the pipe segment, on the side opposite to the crack in stage 1. The reconstruction shows these cracks clearly: The locations and lengths of the cracks are somewhat correct. The orientation of the upper crack is slightly biased, but this bias is insignificant from a practical point of view.

In the third stage (Figure 3, column 3), the first crack (stage 1) is lengthened upward and further extended to two branches, forming a "Y"-shaped crack. The reconstructed surface conductivity traces the "Y" shape of the crack well. The junction of the branches is slightly dislocated, but the size of the crack is again well recovered. In the final stage (Figure 3, column 4), the two small cracks of stage 2 are interconnected, forming a single crack extending from top to the midsection of the pipe segment. Again, the crack is well tracked by the ERT reconstruction, yet a couple of very small defects appear next to it. Note that the cracks in the reconstructed conductivity are thicker than the simulated ones since the inversion mesh is sparser.

In every stage of cracking, the reconstructions are accurate enough for most practical purposes. Deficiencies that are present in the reconstruction are very similar to what is observed in planar sensing skin reconstructions (Hallaji et al., 2014; Jauhiainen et al., 2020; Seppänen et al., 2017). Based on this test case, the nonplanarity does not cause any extra deficiencies into the ERT-based surface sensing of cracks.

3.3.2 | Case 2: Crack detection in pressure vessel

Figure 4 shows the simulated and reconstructed conductivity in each cracking stage in Case 2 where the geometry corresponds to a part of a pressure vessel. Each reconstruction took 15 to 30 min to compute. This increase in computational time is expected, since the inversion mesh of the pressure vessel has more nodes and elements than the pipe segment mesh.

In the first stage (Figure 4, column 1), a very small crack appears at the joint where the diagonal extension connects onto the chamber. In the second stage (Figure 4, column 2), two new cracks form on the side opposite to the crack in stage 1; one of them forms at the joint of the vertical extension and another one forms at the joint of the horizontal extension. In the third stage (Figure 4, column 3), these two cracks are interconnected, forming a single crack that extends from the horizontal extension to the vertical extension. In the final stage (Figure 4, column 4), the crack formed at the first stage lengthens and splits into two branches forming a "Y"-shaped crack.

The reconstructions in Case 2 trace the evolution of the crack pattern well. In all stages of cracking, the reconstruction quality is similar to that in Case 1, although a few more deficiencies are present. This small reduction in quality compared to Case 1 is, however, expected. The surface area of the pressure vessel is 13 times larger than the surface area of the pipe segment in Case 1 and the geometry is far more complex. Overall, the results of Case 2 further confirm the feasibility of the nonplanar 2D ERT to crack detection applications.

3.3.3 | Case 3: Imaging of diffusive phenomena on surface

Figure 5 shows the true conductivity and the reconstruction on each stage in Case 3. In this case, each reconstruction took from 13 to 28 min to compute, which is significantly slower than in Case 1. This is because the smoothness prior has a dense matrix R_Γ, instead of the (very sparse) gradient matrix of TV. This increases the iteration time in the PDPS algorithm that is used by RIPGN.

In the first stage (Figure 5, column 1), a spatially smooth region of low conductivity appears at the middle section of the pipe segment. In the subsequent stages (Figure 5, columns 2–4), the surface area of this region increases and the value within the region decreases further. Each reconstruction reflects the corresponding stage clearly and the deficiencies in these reconstructions are apparent only at the last two stages. These deficiencies, however, look similar to what is observed in 3D and planar 2D ERT studies (Lipponen et al., 2013), and seem to be related to the type of regularization that is used. The simulation clearly demonstrates that ERT imaging of diffusive phenomena is achievable also in nonplanar geometry.

4 | EXPERIMENTAL STUDY

4.1 | Experimental setup and image reconstruction

For the experimental validation of the nonplanar sensing skin, we used a setup where the outer surface of a hollow plastic cube was covered with conductive paint. We refer to the experimental test case as Case 4. The paint was a 1:10 mixture of graphite powder (manufactured by Cretacolor, www.cretacolor.com) and black coating paint (RUBBERcomp, manufactured by Maston, www.maston.fi). Side length of the cube was 0.200 m and bottom of the cube was open (last column in Figure 2). In total, the sensing skin had 32 square-shaped *inner* electrodes (side length 0.012 m). Eight of these electrodes were bent along the edge of the cube so that they were attached on two faces of the cube. The vertical sides had three of these bent electrodes while the top side had four. This particular electrode configuration was chosen in order to utilize all 32 channels of the measurement device.

Here, it is important to note that although the cube-shaped object used in the experiment consists of planar faces, the imaged surface contains also the edges and corners of the cube. In that sense, part of the sensing skin is, in fact, highly nonplanar.

We measured the reference data in the initial stage in which the sensing skin was intact. Subsequently, we simulated the cracking of the underlying structure by cutting the surface of the paint layer with a knife. We generated four different stages of cracking and carried out the ERT measurements corresponding to each of these stages. The same approach to "physically simulating" different stages of cracking has been used previously in cases on planar geometries, for example, in Hallaji et al. (2014) and Seppänen et al. (2017). Based on these studies, the quality of ERT reconstructions is similar between cases where a sensing skin is damaged with knife and where real crack patterns of the same complexity are monitored on the surface of, for example, a concrete beam—this, of course, is the case only when the cracks are large enough to rupture the sensing skin.

As mentioned in Section 2.1, 32 electrodes amount to 991 current measurements. We measured the data with an ERT device manufactured by Rocsole Ltd. (www.rocsole.com). This ERT device samples the currents with 1 MHz frequency, and computes the current amplitudes from the samples using discrete Fourier transform. The device outputs the amplitudes for the excitation potentials and for the measured electric currents. The device selects the amplitude for the excitation potentials automatically. Furthermore, we used the 39 kHz excitation frequency, and to reduce the measurement noise, the current amplitudes that we used in the reconstructions were 1-min time averages. However, the shortest theoretical measurement interval with this excitation frequency is around 40 ms.

Similarly to Cases 1 and 2, we use TV regularization for the crack reconstructions (see Section 3.2). Furthermore, the parameters are the same in the numerical cases. Figure 2c shows the FE mesh used in the inversion. This mesh has 12,278 nodes and 23,965 elements. Note that at every stage, the conductivity of the whole sensing skin, meaning all five sides, is reconstructed, since the mathematical model does not in any way distinguish between the sides of the cube; even the measurements made on the side that is never damaged contribute to the reconstruction.

4.2 | Results and discussion of the experimental study

The top row in Figure 6 shows a photo of the sensing skin at each stage and the two bottom rows show the corresponding reconstructions (Case 4) from two different viewing angles. We highlight the crack made at each stage and the cracks made at the previous stages are darkened; the cracks are very thin (less than 1 mm in thickness) and would otherwise be indistinguishable from the background. Each reconstruction took 8 to 13 min to compute.

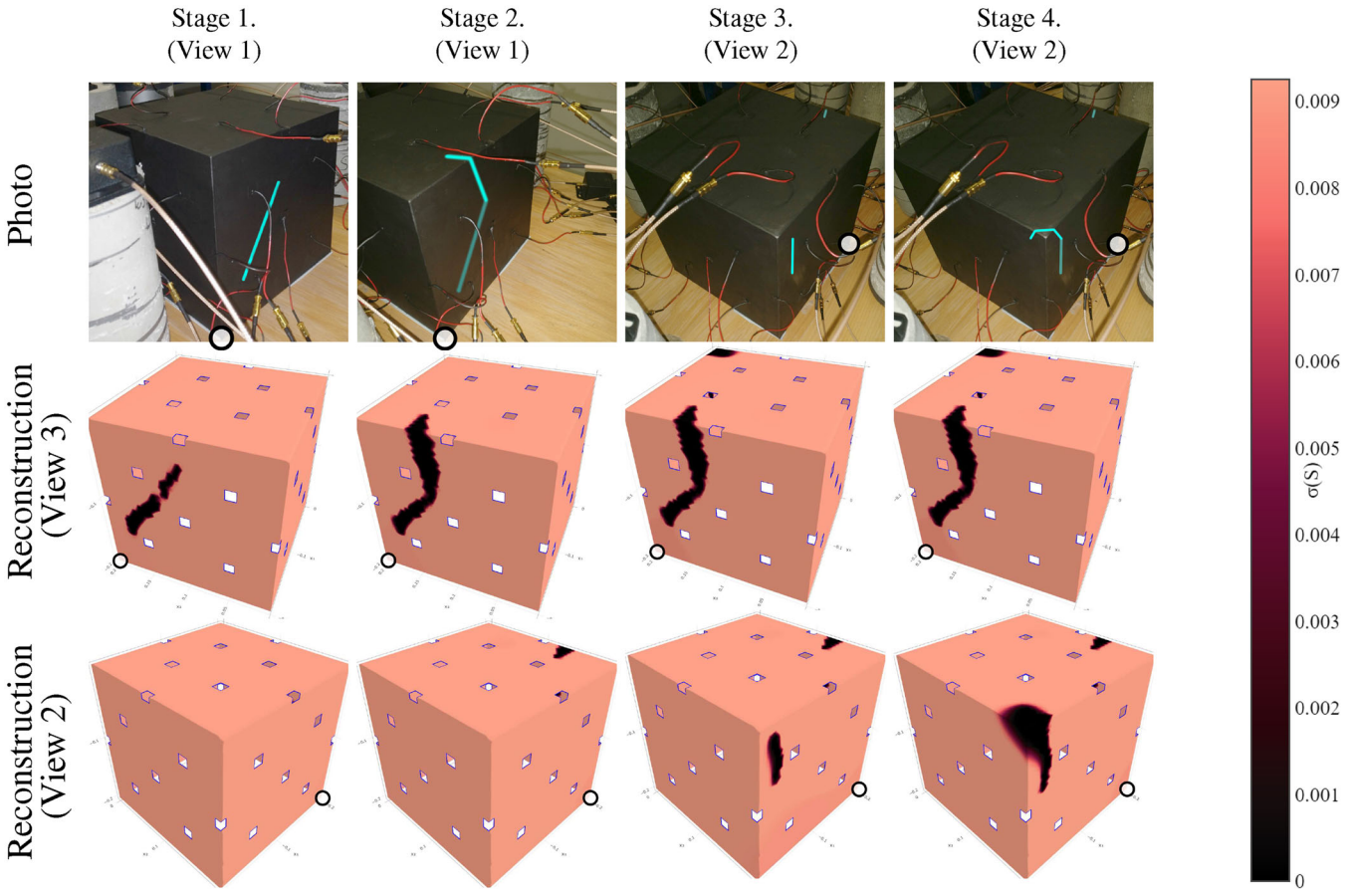

FIGURE 6 Case 4: Photographs of the sensing skin applied on the cubic object in the experimental study (top row) and the respective ERT reconstructions (middle and bottom rows). The photos and reconstructions correspond to four stages of cracking; in the photographs, the cracks at each stage are highlighted and the cracks of the previous stages are darkened. Note that the reconstruction images on the second row also show the side of the cube that has no cracks (View 3). The white circle marks the same corner of the cube in the photographs and in the reconstructions

In the first stage (Figure 6, column 1), we created a diagonal crack on one of the vertical sides of the cube. Reconstruction shows this crack accurately, although a small gap is visible in the reconstruction; the actual crack is fully connected. In the second stage (Figure 6, column 2), we extended the first crack so that it reaches the top side of the cube. The reconstruction shows the location and size of this crack quite accurately, although the curved extension of the crack is wider than the initial crack at stage 1.

In the third stage (Figure 6, column 3), we created a new crack on the adjacent side of the cube while keeping the cracks created at stages 1 and 2 intact. This new crack is clearly visible in the reconstruction. In the final stage (Figure 6, column 4), we extended the crack made on the third stage so that it reaches through the top side to the adjacent side. This extended crack is correctly located by ERT, although the reconstruction shows a blocky area in the corner of the cube. This reconstruction artifact is an expected one, since the electrodes are quite far from the cube corners, and therefore the ERT measurements are less sensitive to conductivity variations in these areas. Note also that the cracks in the reconstructed conductivities are thicker than the actual cracks made on the physical sensing skin. This is, again, partly caused by the sparsity of the finite element (FE) mesh, and partly a result of limited sensitivity of ERT to thickness of the cracks (Hallaji et al., 2014).

Similarly to the simulation studies, the reconstructed conductivities show the crack patterns relatively well. The overall reconstruction quality is, however, slightly worse in this case. This may be due to the modeling errors caused by the inhomogeneity of the paint layer (Smyl et al., 2018) or by the inaccuracy of the electrode locations in the model (Kolehmainen et al., 1997). Furthermore, the detection of the thicknesses of the cracks can possibly be improved upon by modifying the electrode arrangement, although the achieved precision is already sufficient for most practical applications.

5 | CONCLUSIONS

One goal of the SHM research is to develop cost-effective sensor technologies. ERT-based sensing skins have been proposed as cost-effective distributed surface sensing systems for SHM. In the previous studies, the sensing skin sensors have been planar. One of the limitations of the sensing skin technique is that it only provides information on the phenomena on the surface of the structure. Second, although the temporal resolution of ERT is usually excellent, its spatial resolution is rather limited. Furthermore, in the previous studies, the sensing skins have been restricted to planar geometries only.

In this paper, we formulated the computational model for ERT in the case of nonplanar surface sensing. We gave a brief outline of the numerical scheme to reconstruct the nonplanar surface conductivity of the sensing skin. In this scheme, we modeled the relationship between the measured electric currents and the known electric potentials on a surface of an arbitrary object in 3D, and we used this model to formulate a minimization problem that yields the conductivity as the solution. Furthermore, we studied the feasibility of the scheme with three sets of numerical simulations and one set of experimental data.

In the synthetic cases, we acquired highly accurate reconstructions, and we observed only minor artifacts in the reconstructed conductivity. These artifacts were similar to what has been observed in previous planar sensing skins studies. With the measurement data, the reconstruction quality was slightly worse than in synthetic cases but sufficient for most practical applications. Furthermore, we noted that the reconstructions from the measurement data could be improved, for example, by using a more sophisticated model for inhomogeneous background conductivity or by using a different electrode arrangement.

Overall, the reformulation of ERT imaging problem by using a nonplanar surface model proved to be viable; we did not observe any loss of reconstruction quality that could be related to nonplanarity of the sensing skins. We conclude that with the proposed approach, ERT-based sensing skin is viable in monitoring complicated nonplanar surfaces. Furthermore, although our examples were relatively small sized, since ERT is a fully scalable system, in the future, nonplanar sensing skins should allow monitoring of complex industrial structures such as those in aerospace, civil, and mechanical engineering.

ACKNOWLEDGMENTS

This project has received funding from the European Union's Horizon 2020 research and innovation programme under grant agreement number 764810. The research was also funded by the Academy of Finland (Centre of Excellence of Inverse Modelling and Imaging, 2018-2025, project 303801). T. Valkonen has been supported by the Academy of Finland grants 314701 and 320022.

REFERENCES

Alirezaei, H., Nagakubo, A., & Kuniyoshi, Y. (2007). A highly stretchable tactile distribution sensor for smooth surfaced humanoids. In *2007 7th IEEE-RAS International Conference on Humanoid Robots* (pp. 167–173). IEEE.

Alirezaei, H., Nagakubo, A., & Kuniyoshi, Y. (2009). A tactile distribution sensor which enables stable measurement under high and dynamic stretch. In *2009 IEEE Symposium on 3D User Interfaces* (pp. 87–93). IEEE.

Amezquita-Sanchez, J. P., & Adeli, H. (2019). Nonlinear measurements for feature extraction in structural health monitoring. *Scientia Iranica*, *26*(6), 3051–3059.

Bang, S., Park, S., Kim, H., & Kim, H. (2019). Encoder–decoder network for pixel-level road crack detection in black-box images. *Computer-Aided Civil and Infrastructure Engineering*, *34*(8), 713–727.

Brown, B. H. (2003). Electrical impedance tomography (EIT): A review. *Journal of Medical Engineering & Technology*, *27*(3), 97–108.

Chambolle, A., & Pock, T. (2011). A first-order primal-dual algorithm for convex problems with applications to imaging. *Journal of Mathematical Imaging and Vision*, *40*, 120–145.

Cheng, K.-S., Isaacson, D., Newell, J., & Gisser, D. G. (1989). Electrode models for electric current computed tomography. *IEEE Transactions on Biomedical Engineering*, *36*(9), 918–924.

Chossat, J.-B., Shin, H.-S., Park, Y.-L., & Duchaine, V. (2015). Soft tactile skin using an embedded ionic liquid and tomographic imaging. *Journal of Mechanisms and Robotics*, *7*(2), 021008.

Deng, J., Lu, Y., & Lee, V. C.-S. (2020). Concrete crack detection with handwriting script interferences using faster region-based convolutional neural network. *Computer-Aided Civil and Infrastructure Engineering*, *35*(4), 373–388.

Downey, A., Laflamme, S., & Ubertini, F. (2016). Reconstruction of in-plane strain maps using hybrid dense sensor network composed of sensing skin. *Measurement Science and Technology*, *27*(12), 124016.

González, G., Kolehmainen, V., & Seppänen, A. (2017). Isotropic and anisotropic total variation regularization in electrical impedance tomography. *Computers & Mathematics with Applications*, *74*(3), 564–576.

Gutierrez Soto, M., & Adeli, H. (2013). Placement of control devices for passive, semi-active, and active vibration control of structures. *Scientia Iranica*, *20*(6), 1567–1578.

Hallaji, M., & Pour-Ghaz, M. (2014). A new sensing skin for qualitative damage detection in concrete elements: Rapid difference imaging with electrical resistance tomography. *NDT & E International*, *68*, 13–21.

Hallaji, M., Seppänen, A., & Pour-Ghaz, M. (2014). Electrical impedance tomography-based sensing skin for quantitative imaging of damage in concrete. *Smart Materials and Structures*, *23*(8), 085001.

Hampshire, T. A., & Adeli, H. (2000). Monitoring the behavior of steel structures using distributed optical fiber sensors. *Journal of Constructional Steel Research*, *53*(3), 267–281.

He, Y., Qin, J., Cheng, S., & Chen, J. (2020). Estimation of fracture production and water breakthrough locations of multi-stage fractured horizontal wells combining pressure-transient analysis and

electrical resistance tomography. *Journal of Petroleum Science and Engineering*, *194*, 107479.

Hebey, E. (1996). *Sobolev spaces on Riemannian manifolds* (Vol. 1635). Springer Science & Business Media.

Hebey, E. (2000). *Nonlinear analysis on manifolds: Sobolev spaces and inequalities* (Vol. 5). American Mathematical Society.

Hebey, E., & Robert, F. (2008). Sobolev spaces on manifolds. *Handbook of Global Analysis*, *1213*, 375–415.

Hesthaven, J. S., Rozza, G., & Stamm, B. (2016). *Certified reduced basis methods for parametrized partial differential equations* (Vol. 590). Springer.

Hou, T.-C., Loh, K. J., & Lynch, J. P. (2007). Spatial conductivity mapping of carbon nanotube composite thin films by electrical impedance tomography for sensing applications. *Nanotechnology*, *18*(31), 315501.

Hyvonen, N., Seppänen, A., & Staboulis, S. (2014). Optimizing electrode positions in electrical impedance tomography. *SIAM Journal on Applied Mathematics*, *74*(6), 1831–1851.

Isaacson, D. (1986). Distinguishability of conductivities by electric current computed tomography. *IEEE Transactions on Medical Imaging*, *5*(2), 91–95.

Jauhiainen, J., Kuusela, P., Seppänen, A., & Valkonen, T. (2020). Relaxed Gauss–Newton methods with applications to electrical impedance tomography. *SIAM Journal on Imaging Sciences*, *13*(3), 1415–1445.

Kaipio, J., Seppänen, A., Somersalo, E., & Haario, H. (2004). Posterior covariance related optimal current patterns in electrical impedance tomography. *Inverse Problems*, *20*(3), 919.

Kaipio, J., & Somersalo, E. (2006). *Statistical and computational inverse problems* (Vol. 160). Springer Science & Business Media.

Kolehmainen, V., Vauhkonen, M., Karjalainen, P., & Kaipio, J. (1997). Assessment of errors in static electrical impedance tomography with adjacent and trigonometric current patterns. *Physiological Measurement*, *18*(4), 289.

Laflamme, S., Cao, L., Chatzi, E., & Ubertini, F. (2016). Damage detection and localization from dense network of strain sensors. *Shock and Vibration*, *2016*, 2562949.

Lee, J. M. (2000). *Introduction to smooth manifolds. Graduate Texts in Mathematics* (Vol. 218). Springer Science & Business Media. https://link.springer.com/book/10.1007/978-0-387-21752-9

Lee, J. M. (2012). *Introduction to smooth manifolds* (Vol. 218). Springer Science & Business Media.

Lee, J. M. (2018). *Introduction to Riemannian manifolds* (Vol. 2). Springer.

Li, S., Zhao, X., & Zhou, G. (2019). Automatic pixel-level multiple damage detection of concrete structure using fully convolutional network. *Computer-Aided Civil and Infrastructure Engineering*, *34*(7), 616–634.

Li, Z., Park, H. S., & Adeli, H. (2017). New method for modal identification of super high-rise building structures using discretized synchrosqueezed wavelet and Hilbert transforms. *The Structural Design of Tall and Special Buildings*, *26*(3), e1312.

Lipponen, A., Seppänen, A., & Kaipio, J. P. (2013). Electrical impedance tomography imaging with reduced-order model based on proper orthogonal decomposition. *Journal of Electronic Imaging*, *22*(2), 023008.

Liu, J., Yang, X., Lau, S., Wang, X., Luo, S., Lee, V. C.-S., & Ding, L. (2020). Automated pavement crack detection and segmentation based on two-step convolutional neural network. *Computer-Aided Civil and Infrastructure Engineering*, *35*(11), 1291–1305.

Liu, Y.-F., Nie, X., Fan, J.-S., & Liu, X.-G. (2020). Image-based crack assessment of bridge piers using unmanned aerial vehicles and three-dimensional scene reconstruction. *Computer-Aided Civil and Infrastructure Engineering*, *35*(5), 511–529.

Loh, K., Hou, T.-C., Lynch, J., & Kotov, N. (2007). Nanotube-based sensing skins for crack detection and impact monitoring of structures. In *Proceedings of the 6th International Workshop on Structural Health Monitoring*, Stanford, CA, USA (pp. 1685–1692).

Loh, K., Hou, T.-C., Lynch, J. P., & Kotov, N. A. (2009). Carbon nanotube sensing skins for spatial strain and impact damage identification. *Journal of Nondestructive Evaluation*, *28*(1), 9–25.

Loke, M., & Barker, R. (1996). Practical techniques for 3D resistivity surveys and data inversion. *Geophysical Prospecting*, *44*(3), 499–523.

Monk, P. (2003). *Finite element methods for Maxwell's equations*, Oxford University Press. https://doi.org/10.1093/acprof:oso/9780198508885.001.0001

Nayyeri, F., Hou, L., Zhou, J., & Guan, H. (2019). Foreground–background separation technique for crack detection. *Computer-Aided Civil and Infrastructure Engineering*, *34*(6), 457–470.

Ni, F., Zhang, J., & Chen, Z. (2019). Zernike-moment measurement of thin-crack width in images enabled by dual-scale deep learning. *Computer-Aided Civil and Infrastructure Engineering*, *34*(5), 367–384.

Oh, B. K., Kim, K. J., Kim, Y., Park, H. S., & Adeli, H. (2017). Evolutionary learning based sustainable strain sensing model for structural health monitoring of high-rise buildings. *Applied Soft Computing*, *58*, 576–585.

Ozdagli, A. I., & Koutsoukos, X. (2019). Machine learning based novelty detection using modal analysis. *Computer-Aided Civil and Infrastructure Engineering*, *34*(12), 1119–1140.

Perez-Ramirez, C. A., Amezquita-Sanchez, J. P., Valtierra-Rodriguez, M., Adeli, H., Dominguez-Gonzalez, A., & Romero-Troncoso, R. J. (2019). Recurrent neural network model with Bayesian training and mutual information for response prediction of large buildings. *Engineering Structures*, *178*, 603–615.

Rafiei, M. H., & Adeli, H. (2017). A novel machine learning-based algorithm to detect damage in high-rise building structures. *The Structural Design of Tall and Special Buildings*, *26*(18), e1400.

Rashetnia, R. (2017). *Inverse problems in material system monitoring with applications in damage detection and tomography*. [PhD thesis, North Carolina State University].

Rashetnia, R., Hallaji, M., Smyl, D., Seppänen, A., & Pour-Ghaz, M. (2017). Detection and localization of changes in two-dimensional temperature distributions by electrical resistance tomography. *Smart Materials and Structures*, *26*(11), 115021.

Rashetnia, R., Khalaf Alla, O., Gonzalez-Berrios, G., Seppanen, A., & Pour-Ghaz, M. (2018). Electrical resistance tomography–based sensing skin with internal electrodes for crack detection in large structures. *Materials Evaluation*, *76*(10), 1405–1413.

Rodriguez-Lozano, F. J., León-García, F., Gámez-Granados, J. C., Palomares, J. M., & Olivares, J. (2020). Benefits of ensemble models in road pavement cracking classification. *Computer-Aided Civil and Infrastructure Engineering*, *35*(11), 1194–1208.

Rosenberg, S. (1997). *The Laplacian on a Riemannian manifold: an introduction to analysis on manifolds*, London Mathematical Society Student Texts, *31*, 57–58. https://www.cambridge.org/core/books/laplacian-on-a-riemannian-manifold/56F18C2AB0A765A91892E164079A3B74

Rudin, L. I., Osher, S., & Fatemi, E. (1992). Nonlinear total variation based noise removal algorithms. *Physica D: Nonlinear Phenomena*, *60*(1–4), 259–268.

Saito, N. (2017). Notes on the Banach–Nesča–Babuška theorem and Kato's minimum modulus of operators. arXiv preprint arXiv:1711.01533.

Seppänen, A., Hallaji, M., & Pour-Ghaz, M. (2017). A functionally layered sensing skin for the detection of corrosive elements and cracking. *Structural Health Monitoring*, *16*(2), 215–224.

Silvera Tawil, D., Rye, D., & Velonaki, M. (2012). Interpretation of the modality of touch on an artificial arm covered with an EIT-based sensitive skin. *The International Journal of Robotics Research*, *31*(13), 1627–1641.

Smyl, D., Pour-Ghaz, M., & Seppänen, A. (2018). Detection and reconstruction of complex structural cracking patterns with electrical imaging. *NDT & E International*, *99*, 123–133.

Somersalo, E., Cheney, M., & Isaacson, D. (1992). Existence and uniqueness for electrode models for electric current computed tomography. *SIAM Journal on Applied Mathematics*, *52*(4), 1023–1040.

Tallman, T., Gungor, S., Wang, K., & Bakis, C. (2014). Damage detection and conductivity evolution in carbon nanofiber epoxy via electrical impedance tomography. *Smart Materials and Structures*, *23*(4), 045034.

Tallman, T., Gungor, S., Wang, K., & Bakis, C. E. (2015). Damage detection via electrical impedance tomography in glass fiber/epoxy laminates with carbon black filler. *Structural Health Monitoring*, *14*(1), 100–109.

Taylor, M. (2011). *Partial differential equations I: Basic theory*. (Applied mathematical sciences). Springer.

Thomas, A., Kim, J., Tallman, T., & Bakis, C. (2019). Damage detection in self-sensing composite tubes via electrical impedance tomography. *Composites Part B: Engineering*, *177*, 107276.

Valkonen, T. (2019). Block-proximal methods with spatially adapted acceleration. *Electronic Transactions on Numerical Analysis*, *51*, 15–49.

Vauhkonen, P. J. (2004). *Image reconstruction in three-dimensional electrical impedance tomography*. Kuopion yliopisto.

Voss, A. (2020). *Imaging moisture flows in cement-based materials using electrical capacitance tomography*. [PhD thesis, University of Eastern Finland].

Wang, J. (2012). *Geometric structure of high-dimensional data and dimensionality reduction*. Springer.

Worden, K., & Dulieu-Barton, J. M. (2004). An overview of intelligent fault detection in systems and structures. *Structural Health Monitoring*, *3*(1), 85–98.

Wu, H., Zhou, W., Yang, Y., Jia, J., & Bagnaninchi, P. (2018). Exploring the potential of electrical impedance tomography for tissue engineering applications. *Materials*, *11*(6), 930.

Yousef, H., Boukallel, M., & Althoefer, K. (2011). Tactile sensing for dexterous in-hand manipulation in robotics: A review. *Sensors and Actuators A: Physical*, *167*(2), 171–187.

Yu, G., & Adeli, H. (1993). Object-oriented finite element analysis using EER model. *Journal of Structural Engineering*, *119*(9), 2763–2781.

Zhang, A., Wang, K. C., Fei, Y., Liu, Y., Chen, C., Yang, G., Li, J. Q., Yang, E., & Qiu, S. (2019). Automated pixel-level pavement crack detection on 3d asphalt surfaces with a recurrent neural network. *Computer-Aided Civil and Infrastructure Engineering*, *34*(3), 213–229.

Zhang, C., Chang, C.-c., & Jamshidi, M. (2020). Concrete bridge surface damage detection using a single-stage detector. *Computer-Aided Civil and Infrastructure Engineering*, *35*(4), 389–409.

Zhang, X., Rajan, D., & Story, B. (2019). Concrete crack detection using context-aware deep semantic segmentation network. *Computer-Aided Civil and Infrastructure Engineering*, *34*(11), 951–971.

How to cite this article: Jauhiainen J, Pour-Ghaz M, Valkonen T, Seppänen A. Nonplanar sensing skins for structural health monitoring based on electrical resistance tomography. *Comput Aided Civ Inf*. 2021;*36*:1488–1507.
https://doi.org/10.1111/mice.12689

APPENDIX: IMPLEMENTATION DETAILS

Similarly to Euclidean spaces (Voss, 2020), we derive a FE approximation for (1). Although (1) looks identical to the Euclidean counterpart, the definitions of the operators in (1) are more involved, containing calculations based on the Riemannian metric g.

The FE approximation relies on the weak formulation of (1). The well-posedness of this weak formulation has been previously shown for (u^p, U^p) (i.e., the potential measurement setup) (Somersalo et al., 1992) in Euclidean spaces, however for (u^p, I^p) (i.e., the current measurement setup), no previous work exists; we will show the well-posedness of the weak formulation for (u^p, I^p) in the manifold setting, which also extends to the Euclidean setting.

Initially, we take g as an arbitrary metric on M. However, to see how to compute the FE approximation through integration in $\mathbb{R}^2$, we need to fix g. In this case, to properly account for the shape of M in $\mathbb{R}^3$, we take g as the metric induced on M by the natural metric on $\mathbb{R}^3$ (Lee, 2003, 2018). Namely, for tangents w_1, w_2 on the tangent plane T_xM at a point x (illustrated in Figure A1), it is defined by $g(w_1, w_2) := \tilde{g}(d\phi(w_1), d\phi(w_2))$, where $\phi : M \to \mathbb{R}^3$ is the inclusion map $\phi(x) := x$ and $\tilde{g} = (dx^1)^2 + (dx^2)^2 + (dx^3)^2$ is the Euclidean metric in $\mathbb{R}^3$.

The solutions (u^p, I^p) of (1) comprise a twice continuously differentiable function $u^p \in C^2 := C^2(M)$ and a vector $I^p \in \mathbb{R}^L$ with components I^p_k, $k = 1, \dots, L$. We denote $(u^p, I^p) \in C^2 := C^2(M) \oplus \mathbb{R}^L$. We will show that the FE approximation of (1), however, satisfies the weak formulation,

$$B((u^p, I^p), (v, V)) = L((v, V)), \quad \forall (v, V) \in H \qquad \text{(A1)}$$

where B is bilinear and L is linear. The space

$$H := H^1(M) \oplus \mathbb{R}^L$$

where $H^1(M)$ is a Hilbert space of (once) weakly differentiable functions. We define it as the completion of $C^\infty(M)$ with respect to the norm $\|\cdot\|_{H^1(M)}$ (Hebey, 2000, Chapter 10). It corresponds to the common space $H^1(\Omega)$ also used with planar CEM (Somersalo et al., 1992). The natural norm for this space is (Hebey, 1996, 2000; Somersalo et al., 1992)

$$\|(v,V)\|_H^2 = \|v\|_{H^1(M)}^2 + \|V\|_{\mathbb{R}^L}^2 \tag{A2}$$

where the inner products inducing the individual norms are

$$\langle u, v\rangle_{H^1(M)} = \int_M uv dS + \int_M \langle \nabla u, \nabla v\rangle_g dS$$

and

$$\langle U, V\rangle_{\mathbb{R}^L} = \sum_{k=1}^L U_k V_k$$

In the following lemmas, we assume that the model (1) has at least two electrodes, that is, $L \geq 2$.

Lemma A1. *Suppose that $\zeta_k > 0$ is constant on ∂M_{e_k} $\forall k$, the part of ∂M corresponding to electrode k. Then the PDE (1) admits a weak formulation (A1), where the bilinear operator $B : H \times H \to \mathbb{R}$ and the linear operator $L : H \to \mathbb{R}$ are given by*

$$B((u^p, I^p),(v,V)) = \int_M \sigma\langle \nabla v, \nabla u^p\rangle_g dS + \sum_k^L \frac{1}{\zeta_k}\int_{\partial M_{e_k}} u^p v d\tilde{S}$$

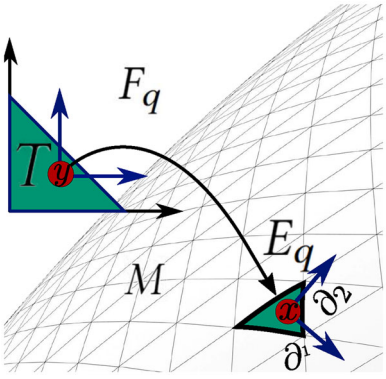

FIGURE A1 Manifold M is described locally on T by diffeomorphism F_q. At point x, the tangents ∂_1 and ∂_2 set the basis for the tangent plane T_xM

$$-\sum_k^L \frac{1}{\zeta_k}\int_{\partial M_{e_k}} u^p V_k d\tilde{S} + \sum_k^L I_k^p V_k \tag{A3}$$

and

$$L(v,V) = \sum_k^L \frac{1}{\zeta_k}\int_{\partial M_{e_k}} U_k(v - V_k) d\tilde{S}$$

Proof. Suppose that (u^p, I^p) solves (1). We need to show that it solves (A1). So let $(v,V) \in H$ be arbitrary. We define $X := \sigma\nabla u^p$. Applying $\int_M \cdot v dS$ to (1a) we get

$$-\int_M v\nabla\cdot(\sigma\nabla u^p) dS = -\int_M v\nabla\cdot X dS = 0 \tag{A4}$$

where dS is the Riemannian volume corresponding to the metric g on M. Denoting by $d\tilde{S}$ the Riemannian volume on ∂M, using the product rule, the divergence theorem on Riemannian manifolds (Wang, 2012, Appendix A), and (1b) to replace $\sigma\langle\nabla u^p, \hat{n}\rangle_g$, we obtain

$$\begin{aligned}
0 &= \int_M v\nabla\cdot X dS = \int_M \langle\nabla v, X\rangle_g dS - \int_{\partial M} v\langle X, \hat{n}\rangle_g \, d\tilde{S} \\
&= \int_M \langle\nabla v, \sigma\nabla u^p\rangle_g dS - \int_{\partial M} v\langle\sigma\nabla u^p, \hat{n}\rangle_g \, d\tilde{S} \\
&= \int_M \sigma\langle\nabla v, \nabla u^p\rangle_g dS - \sum_k^L \int_{\partial M_{e_k}} v\sigma\langle\nabla u^p, \hat{n}\rangle_g \, d\tilde{S} \\
&= \int_M \sigma\langle\nabla v, \nabla u^p\rangle_g dS - \sum_k^L \int_{\partial M_{e_k}} v(U_k^p - u^p)/\zeta_k \, d\tilde{S}
\end{aligned} \tag{A5}$$

Equations (1b) and (1c) both hold for each $k = 1, \ldots, L$ and define the vectors $U^p, I^p \in \mathbb{R}^L$. By multiplying each component U_k^p of U^p by V_k/ζ_k, where V_k is a component of a test vector $V \in \mathbb{R}^L$, integrating over ∂M_{e_k}, and summing over $k = 1, \ldots, L$, we get

$$\begin{aligned}
&\sum_k^L \int_{\partial M_{e_k}} u^p(x) V_k/\zeta_k \tilde{V} + \int_{\partial M_{e_k}} \sigma\langle\nabla u^p(x), \hat{n}\rangle_g V_k \tilde{V} \\
&\quad - \int_{\partial M_{e_k}} U_k^p V_k/\zeta_k d\tilde{S} = 0
\end{aligned} \tag{A6}$$

Since V_k is constant on ∂M_{e_k}, $\int_{\partial M_{e_k}} \sigma\langle\nabla u^p(x), \hat{n}\rangle_g V_k d\tilde{S} = \int_{\partial M_{e_k}} \sigma\langle\nabla u^p(x), \hat{n}\rangle_g d\tilde{S} V_k = -I_k^p V_k$. Subtracting (A6) from (A5) and plugging in I_k^p gives

$$0 - 0 = \int_M \sigma\langle\nabla v, \nabla u^p\rangle_g dS - \sum_k^L \int_{\partial M_{e_k}} v(U_k^p - u^p)/\zeta_k \, d\tilde{S}$$

$$-\left(\sum_k^L \int_{\partial M_{e_k}} u^p(x)V_k/\zeta_k - U_k^p V_k/\zeta_k d\tilde{S} - I_k^p V_k\right)$$
$$= \int_M \sigma\langle\nabla v, \nabla u^p\rangle_g dS$$
$$+ \sum_k^L \left(\int_{\partial M_{e_k}} u^p(v - V_k)/\zeta^k + U_k(V_k - v)/\zeta^k d\tilde{S} + I_k^p V_k\right)$$

Finally, since we assume ζ_k is constant, by subtracting $\sum_k^L \int_{\partial M_{e_k}} U_k(V_k - v)/\zeta^k d\tilde{S}$ we get (A1). □

The next lemma shows that the weak formulation (A1) is well-posed, meaning that the solution (u^p, I^p) exists and is unique, and B is continuous, leading eventually to the invertibility of the linear system of the FE approximation. For the simplicity, we assume that the boundary ∂M of M is C^∞. However, the arguments that we use in the following proofs should extend to domains with boundaries of lesser smoothness.

Now, if we were solving for (u^p, U^p) instead of (u^p, I^p), we could follow the treatment in Somersalo et al. (1992) by replacing relevant theorems on Sobolev spaces by their (compact Riemannian) manifold counterparts. However, no well-posedness proof for the weak formulation of (u^p, I^p) exists. To prove the well-posedness for (u^p, I^p), we show that the conditions of the Banach–Nesča–Babuška theorem (BNB) hold for B and that B is continuous. The Euclidean case will follow as long as the domain for $u^p(x)$ is bounded.

Lemma A2. *Suppose that $0 < \sigma_m \leq \sigma(x) \leq \sigma_M < \infty$ is integrable on compact connected Riemannian manifold (M, g) and with a C^∞ boundary ∂M. Then (A1) is well-posed.*

Proof. For the proof, to avoid confusion between variables and not carry the index p, we write (w, W) in place of (u^p, I^p). According to BNB (Hesthaven et al., 2016, Theorem A.4) (see also Saito, 2017, Theorem 1), since H is a reflexive Banach space (Hebey & Robert, 2008, Proposition 2.1)—note that H also a Hilbert space (Hebey, 2000, Proposition 2.1)—there exists a unique solution $(w, W) \in H$ to the problem (A1) if

$$\sup_{(v,V)\in H} \frac{B((w,W),(v,V))}{\|(v,V)\|_H} \geq \beta\|(w,W)\|_H \text{ for some } \beta > 0 \tag{A7a}$$

$$(\forall (w,W) \in H, B((w,W),(v,V)) = 0) \Rightarrow ((v,V) = 0) \tag{A7b}$$

First, however, similarly to Somersalo et al. (1992), we will show that

$$\|(v,V)\|_*^2 := \int_M \langle\nabla v, \nabla v\rangle_g dS + \|v\|_{\partial M_e}^2 + \|V\|_{\mathbb{R}^L}^2$$

where $\|v\|_{\partial M_e}^2 := \sum_k^L \int_{\partial M_{e_k}} v^2 d\tilde{V}$, is a norm equivalent to (A2), that is, there exists constants $\lambda, \Lambda > 0$ such that

$$\Lambda\|(v,V)\|_* \geq \|(v,V)\|_H \geq \lambda\|(v,V)\|_* \quad \forall (v,V) \in H \tag{A8}$$

To see that the first inequality of (A8) holds, by the continuous embedding $H^{1/2}(\partial M) \subset L^2(\partial M)$ (Taylor, 2011, Definition 1.4, Chapter 4) for some $C_1, C_2 > 0$,

$$\|v\|_{\partial M_e}^2 \leq \|v\|_{L^2(\partial M)}^2 \leq C_1\|v\|_{H^{1/2}(\partial M)}^2 \leq C_2\|v\|_{H^1(M)}^2$$

Since $\langle\nabla v, \nabla v\rangle_g \geq 0$, we thus obtain for some $\Lambda > 0$ that $\|(v,V)\|_*^2 \leq \Lambda^2(\|v\|_{H^1(M)}^2 + \|V\|_{\mathbb{R}^L}^2) = \Lambda^2\|v\|_H^2$.

To verify the second inequality of (A8), assume that the claim is not true. Then we can take a sequence $\{(v^n, V^n)\}_{n=1}^\infty \in H$, so that $\|(v^n, V^n)\|_H = 1$ and $\|(v^n, V^n)\|_* < 1/n$. Now, according to the compact embedding theorem on Sobolev spaces on manifolds (Taylor, 2011, Proposition 4.4, Chapter 4), v^n contains a converging subsequence $v^{n_i} \to v \in L^2(M)$, $n_i > n_{i-1}$, and $v \in L^2(M)$. Since $\frac{1}{n_i} > \|(v^{n_i}, V^{n_i})\|_*$, we have that

$$\frac{1}{n_i^2} > \int_M \langle\nabla v^{n_i}, \nabla v^{n_i}\rangle_g dS,\ \frac{1}{n_i} > \|v^{n_i}\|_{\partial M_e}, \text{ and } \frac{1}{n_i} > \|V^{n_i}\|_{\mathbb{R}^L} \tag{A9}$$

The first inequality implies that v^{n_i} forms a converging sequence in $H^1(M)$, which satisfies $\int_M \langle\nabla v^{n_i}, \nabla v^{n_i}\rangle_g dS \to 0$. Applying Poincaré (Hebey, 2000, Theorem 2.10) and Hölder inequalities (follows directly from Young's inequality) shows for constants $c_1 \in \mathbb{R}$ and $c_2 > 0$ that

$$\|v^{n_i} - c_1\|_{L^1(M)}^2 \leq c_2\|\nabla v^{n_i}\|_{L^1(M)}^2 \leq c_2\|\nabla v^{n_i}\|_{L^2(M)}^2\|1\|_{L^2(M)}^2$$

and since $\|\nabla v^{n_i}\|_{L^2(M)}^2\|1\|_{L^2(M)}^2 \to 0$, v^{n_i} converges to the constant c_1 in $L^1(M)$. Further, since $v^{n_i} \to v \in L^2(M)$, using Hölder's inequality again shows that $\|v^{n_i} - v\|_{L^1(M)} \leq \|v^{n_i} - v\|_{L^2(M)}\|1\|_{L^2(M)} \to 0$, meaning that v^{n_i} also converges to the same v in $L^1(M)$, confirming that indeed $v = c_1$, that is, v is constant almost everywhere. Now, since v is a.e. constant and $v|_{\partial M} \in L^2(\partial M)$, the second inequality in (A9) implies that $v^{n_i} \to 0$, that is, $c_1 = 0$. The final inequality in (A9) implies that $V^{n_i} \to 0$, that is,

$V = 0$. Since $v^{n_i} \to 0$ and $V^{n_i} \to 0$, $\|(v^{n_i}, V^{n_i})\|_H \to 0$, contradicting $\|(v^{n_i}, V^{n_i})\|_H = 1$.

To see that (A7a) holds, start by denoting $s_k = \int_{\partial M_{e_k}} 1 d\tilde{S}$, $a := \max\{\zeta_1^{-1}, \zeta_2^{-1}, \dots, s_1^2\zeta_1^{-1}, s_2^2\zeta_2^{-1}, \dots\}$, and $c := a \min\{1/a, \sigma_m, \zeta_1^{-1}, \zeta_2^{-1}, \dots\}$. If $(w, W) = (0, 0)$, then (A7a) clearly holds. If $(w, W) \neq (0, 0)$, then pick a function $(\hat{v}, \hat{V}) \in H$ that satisfies $\hat{v} = 2aw$ and $\hat{V}_k = W_k + \frac{1}{\zeta_k}\int_{\partial M_{e_k}} w d\tilde{V}$.

Plugging $(\tilde{v}, \tilde{V})$ into (A1) and simplifying gives

$$
\begin{aligned}
B((w, W), (\hat{v}, \hat{V})) &= 2a \int_M \sigma \langle \nabla w, \nabla w \rangle_g dS \\
&+ \sum_k^L \frac{2a}{\zeta_k} \int_{\partial M_{e_k}} w^2 d\tilde{S} - \sum_k^L \left(\frac{1}{\zeta_k} \int_{\partial M_{e_k}} w d\tilde{S} \right)^2 + \sum_k^L W_k^2 \\
&\geq 2a \int_M \sigma \langle \nabla w, \nabla w \rangle_g dS + \sum_k^L \frac{2a}{\zeta_k} \int_{\partial M_{e_k}} w^2 d\tilde{S} \\
&- \sum_k^L \frac{a}{\zeta_k} \int_{\partial M_{e_k}} w^2 d\tilde{S} + \sum_k^L W_k^2 \\
&\geq c \left(\int_M \langle \nabla w, \nabla w \rangle_g dS + \sum_k^L \int_{\partial M_{e_k}} w^2 d\tilde{S} + \sum_k^L W_k^2 \right) \\
&= c \|(w, W)\|_*^2
\end{aligned}
$$

Denoting $b := 2 \max\{1, 2a^2, |e_1|^2\zeta_1^{-2}, |e_2|^2\zeta_2^{-2}, \dots\}$,

$$
\begin{aligned}
\|(\hat{v}, \hat{V})\|_*^2 &\leq 4a^2 \Big(\int_M \langle \nabla w, \nabla w \rangle_g dS + \|w\|_{\partial M_e}^2 \Big) \\
&+ \sum_k 2 \Big(W_k^2 + \big(\frac{1}{\zeta_k} \int_{\partial M_{e_k}} v dx \big)^2 \Big) \\
&\leq 4a^2 \Big(\int_M \langle \nabla w, \nabla w \rangle_g dS + \|w\|_{\partial M_e}^2 \Big) \\
&+ \sum_k \Big(2W_k^2 + \frac{2s_k^2}{\zeta_k^2} \int_{\partial M_{e_k}} v^2 dx \Big) \\
&\leq 2b \Big(\int_M \langle \nabla w, \nabla w \rangle_g dS + \|w\|_{\partial M_e}^2 + W_{\mathbb{R}^L}^2 \Big) \\
&= 2b \|(w, W)\|_*^2
\end{aligned}
$$

Combining the above shows that

$$
\sup_{(v,V) \in H} \frac{B((w,W),(v,V))}{\|(v,V)\|_H} \geq \frac{c\|(w,W)\|_*^2}{\Lambda \|(\hat{v},\hat{V})\|_*} \geq \frac{c\|(w,W)\|_*^2}{\Lambda \sqrt{2b} \|(w,W)\|_*} \geq \frac{c\|(w,W)\|_H}{\sqrt{2b}\Lambda^2}
$$

To see that (A7b) holds, assume the contrary, that is, there exists a $(v, V) \neq 0$ so that $B((w, W), (v, V)) = 0$ holds for all (w, W). If $V = 0$ choose $(w, W) = (v, 0)$. If $V \neq 0$ choose $(w, W) = (0, V)$. Both scenarios show that $B((w, W), (v, V)) \neq 0$ with the chosen (w, W), that is, that $B((w, W), (v, V)) = 0$ does not hold for all (w, W), which is a contradiction, meaning that the condition must hold.

Finally, to see that B is continuous, that is, $B((w, W), (v, V)) \leq C\|(w, W)\|_H \|(v, V)\|_H$ for some $C > 0$, observe that

$$
\begin{aligned}
-\sum_k^L \frac{1}{\zeta_k} \int_{\partial M_{e_k}} w V_k d\tilde{S} &\leq \sum_k^L \Big| \frac{1}{\zeta_k} \int_{\partial M_{e_k}} w V_k d\tilde{S} \Big| \\
&\leq a \|w\|_{\partial M_e} \|V\|_{\mathbb{R}^L} \leq a \|(w, W)\|_* \|(v, V)\|_*
\end{aligned}
$$

Denoting $\tilde{c} := \max\{1, \sigma_M, \zeta_1^{-1}, \zeta_2^{-1}, \dots\}$, clearly,

$$
\begin{aligned}
B((w, W), (v, V)) &\leq \tilde{c} \|(w, W)\|_* \|(v, V)\|_* \\
-\sum_k^L \frac{1}{\zeta_k} \int_{\partial M_{e_k}} w V_k d\tilde{S} &\leq (\tilde{c} + a) \|(w, W)\|_* \|(v, V)\|_* \\
&\leq (\tilde{c} + a) \lambda^{-2} \|(w, W)\|_H \|(v, V)\|_H
\end{aligned}
$$

This finishes the proof. □

For the next lemma, we will replace u^p and I_k^p by their FE approximations $u^p = \sum_j^N u_j^p v_j$ and $I^p = \sum_{j=1}^{L-1} (\tilde{I}_j n_j)$, where we allow v_j to be an arbitrary FE basis function. For $I^p \in \mathbb{R}^L$, we fix basis vectors $n_j \in \mathbb{R}^L$ so that we can utilize Kirchhoff's law to eliminate one of the components: we choose vectors $n_j \in \mathbb{R}^L$ such that the components of n_j are $(n_j)_1 = 1$, $(n_j)_{j+1} = -1$, and otherwise $(n_j)_k = 0$. This fixes the value of the I_1^p so that $I_1^p = -\sum_{i=2}^L I_i^p$. Indeed, due to the Kirchhoff's law, we only have $L - 1$ unknown currents. Note also that n_j no longer appears in the lemma, since the value is easy to determine.

Lemma A3. *Replace H by a finite dimensional subspace*

$$
H_N = \text{span}\{(v_1, 0), \dots, (v_N, 0), (0, n_1), \dots, (0, n_{L-1})\}
$$

Then (A1) admits the presentation $D\theta = \bar{U}$, where $D \in \mathbb{R}^{(N+L-1)\times(N+L-1)}$ with

$$
D = \begin{bmatrix} D_1 & 0 \\ D_2 & D_3, \end{bmatrix} \quad (D_3)_{i,j} = \begin{cases} 2, & i = j \\ 1, & \text{otherwise} \end{cases}
$$

$$
(D_2)_{i,j} = \frac{1}{\zeta_{i+1}} \int_{\partial M_{e_{i+1}}} v_j d\tilde{S} - \frac{1}{\zeta_1} \int_{\partial M_{e_1}} v_j d\tilde{S}
$$

$$
(D_1)_{i,j} = \int_M \sigma \langle \nabla v_i, \nabla v_j \rangle_g dS + \sum_k^L \frac{1}{\zeta_k} \int_{\partial M_{e_k}} v_j v_i d\tilde{S}
$$

and $\bar{U} \in \mathbb{R}^{N+L-1}$

$$(\bar{U})_i = \begin{cases} \sum_k^L \frac{U_k}{\zeta_k} \int_{\partial M_{e_k}} v_i d\tilde{S}, & i \leq N \\ \frac{U_{i+1}}{\zeta_{i+1}} \int_{\partial M_{e_{i+1}}} 1 d\tilde{S} - \frac{U_1}{\zeta_1} \int_{\partial M_{e_1}} 1 d\tilde{S}, & \text{otherwise} \end{cases}$$

The vector $\theta = (\bar{u}^p, \bar{I}^p)$*, where* $(\bar{u}^p)_i = u_i^p$*,* $(\bar{I}^p)_i = \tilde{I}_i^p$ *contains the coefficients of the FE approximations for* u^p *and* I_k^p*. Furthermore, the problem is well-posed, Galerkin orthogonality holds and for the exact solution* $(\hat{u}^p, \hat{I}^p)$ *and some constant* $C > 0$ *we have*

$$\|(\hat{u}^p - u^p, \hat{I}^p - I^p)\|_H \leq C \inf_{(v,V)\in H_N} \|(\hat{u}^p - v, \hat{I}^p - V^p)\|_H \tag{A10}$$

Proof. Since B is continuous and since BNB holds for B, by applying the Cea's lemma (Monk, 2003, Lemma 2.37), we see that the problem is well-posed also in H_N and the Galerkin orthogonality and (A10) hold for the solution (u^p, I^p).

Plugging in the expression for u^p and I^p into (A3) gives N equations corresponding to each $(v, V) = (v_i, 0)$:

$$\begin{aligned} &\int_M \sigma \langle \nabla v_i, \nabla \sum_j^N u_j^p v_j \rangle_g dS + \sum_k^L \frac{1}{\zeta_k} \int_{\partial M_{e_k}} \sum_j^N u_j^p v_j v_i d\tilde{S} \\ &= \sum_j^N u_j^p \left(\int_M \sigma \langle \nabla v_i, \nabla v_j \rangle_g dS + \sum_k^L \frac{1}{\zeta_k} \int_{\partial M_{e_k}} v_j v_i d\tilde{S} \right) \\ &= \sum_k^L \frac{1}{\zeta_k} \int_{\partial M_{e_k}} U_k v_i d\tilde{S} \end{aligned}$$

which can be written with the matrix D_1 and vectors $\bar{u}$ and $(\bar{U}_1)_i = \sum_k^L \frac{U_k}{\zeta_k} \int_{\partial M_{e_k}} v_i d\tilde{S}$ as $D_1 \bar{u} = \bar{U}_1$. Further, $(v, V) = (0, n_i)$ gives additional $L - 1$ equations:

$$\begin{aligned} &- \sum_k^L \frac{1}{\zeta_k} \int_{\partial M_{e_k}} \sum_j^N u_j^p v_j n_i d\tilde{S} + \sum_k^L I_k^p V_k \\ &= - \sum_k^L \frac{1}{\zeta_k} \int_{\partial M_{e_k}} \sum_j^N u_j^p v_j n_i d\tilde{S} + \sum_k^L (\sum_j^{L-1} \tilde{I}_j n_j)_k (n_i)_k \\ &= \sum_j^N \left(\frac{u_j^p}{\zeta_{i+1}} \int_{\partial M_{e_{i+1}}} v_j d\tilde{S} - \frac{u_j^p}{\zeta_1} \int_{\partial M_{e_1}} v_j d\tilde{S} \right) \\ &+ \sum_j^{L-1} \tilde{I}_j \sum_k^L (n_j)_k (n_i)_k = - \sum_k^L \frac{1}{\zeta_k} \int_{\partial M_{e_k}} U_k (n_i)_k d\tilde{S} \end{aligned}$$

which can be expressed with D_2, D_2, $\bar{u}$, $\bar{U}_1$, $\bar{I}$, and $(\bar{U}_2)_i = - \sum_k^L \frac{1}{\zeta_k} \int_{\partial M_{e_k}} U_k (n_i)_k d\tilde{S} = \frac{U_{i+1}}{\zeta_{i+1}} \int_{\partial M_{e_{i+1}}} 1 d\tilde{S} - \frac{U_1}{\zeta_1} \int_{\partial M_{e_1}} 1 d\tilde{S}$ as $D_2 \bar{u} = \bar{U}_1$ and $D_3 \bar{I} = \bar{U}_2$. Finally, by combining the results we have

$$\begin{bmatrix} D_1 & 0 \\ D_2 & D_3 \end{bmatrix} \begin{bmatrix} \bar{u} \\ \bar{I} \end{bmatrix} = \begin{bmatrix} \bar{U}_1 \\ \bar{U}_2 \end{bmatrix}$$

This finishes the proof. □

A.1 | Computing the FE approximation

In Lemma A3, we derived the matrix presentation of the FE approximation. This matrix form, however, is abstract in the sense that the integrals are still presented in M and ∂M.

To proceed further, we consider specific maps to the manifold M. We define the elementary triangle by $T := \{y \in \mathbb{R}^2 \,|\, y^1, y^2 \geq 0,\ y^1 + y^2 \leq 1\}$ and denote the boundary segments of this triangle by $\partial_1 T := \{y \in T \,|\, y^2 = 0\}$, $\partial_2 T := \{y \in T \,|\, y^1 = 0\}$, and $\partial_3 T := \{y \in T \,|\, y^1 = y^2\}$. Further, we assume that there exists a triangulation of M, meaning that:

- There are domains E_q (in practice "geodesic triangles," compare Figure 1), such that $M = E_1 \cup E_1 \ldots \cup E_K$.
- For each q there exists an orientation preserving diffeomorphism $F_q(T) = E_q$ (i.e., $F_q : T \to E_q$ and $F_q^{-1} : E_q \to T$ are differentiable bijections and the Jacobian determinant of F_q is positive). Intuitively, this means that T can be morphed smoothly to E_q and E_q back to T through F_q and F_q^{-1}, so that the right-hand (or left-hand) rule is preserved.
- The subdomains E_q and E_r for $q \neq r$ may only intersect at the boundaries.
- For each electrode e_k some collection $\mathcal{B}_k$ of r and β correspond to the boundary segment of e_k, that is, $\partial M_{e_k} = \bigcup_{(r,\beta)\in\mathcal{B}_k} F_r(\partial_\beta T)$, where $(q, \alpha), (r, \beta) \in \mathcal{B}_k$, $(q, \alpha) \neq (r, \beta)$, the subdomains $F_q(\partial_\alpha T) \subset \partial M$ and $F_r(\partial_\beta T) \subset \partial M$ may only intersect at the end points.

In addition, we need a presentation for the metric g on T. Recall that g has the specific form $g(w_1, w_2) = \tilde{g}(d\phi(w_1), d\phi(w_2))$. Clearly, this metric has a matrix presentation $g = J_q^T J_q$ (Rosenberg, 1997, pp. 57–58) on T, where J_q is the Jacobian matrix of F_q. Similarly, if $\gamma_\alpha(t)$ is a curve that maps [0,1] to one of the boundaries $\partial_\alpha T$, then $g_\omega(w) = g(d\gamma_\alpha(w))$ has a presentation $g_\omega = J_{q_{\gamma\alpha}}^T J_{q_{\gamma\alpha}}$ in [0,1], where $J_{q_{\gamma\alpha}}$ is the Jacobian of $F_q(\gamma_\alpha(t))$.

Now we derive the exact forms for the integrals of (A3) in terms of T and the interval [0,1]. The next lemma combined with Lemma A3 finally allows us to calculate the

matrices and vectors of the FE system that determines $I(\sigma)$ in (6). The RIPGN algorithm (Jauhiainen et al., 2020) utilizes these vectors and matrices to solve (6).

Lemma A4. *Assume that there exists a triangulation $\{E_q\}$ of M. The integrals in Lemma A3 have the following presentations;*

$$\int_M \sigma\langle\nabla v_i, \nabla v_j\rangle_g dS$$

$$= \sum_q \int_T \sigma(F_q(y))(\nabla_y v_i(F_q(y)))^T g^{-1}(\nabla_y v_j(F_q(y)))\sqrt{|g|}dy$$

$$\sum_k^L \frac{1}{\zeta_k}\int_{\partial M_{e_k}} v_j v_i d\tilde{S}$$

$$= \sum_k^L \sum_{(q,\alpha)\in\mathcal{I}(i,j,k)} \frac{U_k}{\zeta_k}\int_0^1 v_j(F_q(\gamma_\alpha(t)))v_i(F_q(\gamma_\alpha(t)))\sqrt{g_\omega}dt$$

$$\frac{U_k}{\zeta_k}\int_{\partial M_{e_k}} v_j d\tilde{S} = \sum_{(q,\alpha)\in\mathcal{I}(j,k)} \frac{U_k}{\zeta_k}\int_0^1 v_j(F_q(\gamma_\alpha(t)))\sqrt{g_\omega}dt$$

and

$$\frac{U_k}{\zeta_k}\int_{\partial M_{e_k}} 1 d\tilde{S} = \sum_{(q,\alpha)\in\mathcal{I}(k)} \frac{U_k}{\zeta_k}\int_0^1 \sqrt{g_\omega}dt$$

where $y := (y^1, y^2) \in T$, $dy := dy^1 dy^2$, g^{-1} is a matrix representing the coefficients of g^{ij}, $\nabla_y f$ is the gradient of f with respect to the variable $y \in T \subset \mathbb{R}^2$, and

$$\mathcal{I}(i,j,k) := \{(q,\alpha) \mid \partial F_q(\partial_\alpha T) \text{ is under an electrode } k, v_i(F_q(\partial_\alpha T)) \neq \{0\}, \text{ and } v_j(F_q(\partial_\alpha T)) \neq \{0\}\},$$

$$\mathcal{I}(i,k) := \{(q,\alpha) \mid \partial F_q(\partial_\alpha T) \text{ is under an electrode } k \text{ and } v_i(F_q(\partial_\alpha T)) \neq \{0\}, \text{ and}$$

$$\mathcal{I}(k) := \{(q,\alpha) \mid \partial F_q(\partial_\alpha T) \text{ is under an electrode } k\}$$

Proof. By assumption T and ∂T are compact, F_q are diffeomorphic, $\partial M_{e_k} = \bigcup_{(r,\beta)\in\mathcal{B}_k} F_r(\partial_\beta T)$ and $M = E_1 \cup E_1 \ldots \cup E_K$, where $q \neq r$ and $(q,\alpha) \neq (r,\beta)$ only intersect at their boundaries, the conditions of (Lee, 2003, Proposition 10.21) are met for M and for each ∂M_{e_k}, and the integrals of (A1) defined in M and in ∂M_{e_k} can be expressed as sums of Riemannian integrals in $\mathbb{R}$ or $\mathbb{R}^2$ over the sets T and ∂T, that is, for $f : M \to \mathbb{R}$ and $\tilde{f} : \partial M_{e_k} \to \mathbb{R}$, that is,

$$\int_M f dS = \sum_q \int_T F_q^*(f dS) = \sum_q \int_T (f \circ F_q)\sqrt{|g|}dy \quad \text{and}$$

$$\int_{\partial M_{e_k}} \tilde{f} d\tilde{S} = \sum_{(r,\beta)\in\mathcal{B}_k} \int_{\partial_\beta T} F_r^*(\tilde{f} d\tilde{V}) = \sum_{(r,\beta)\in\mathcal{B}_k} \int_{\partial_\beta T} (\tilde{f} \circ F_r)\sqrt{|g_\omega|}d\tilde{y}$$

where $y \in T$ and $\tilde{y} \in \partial_\beta T$ (Lee, 2012, Proposition 11.25, Proposition 15.31, and p. 402).

Since g^{ij} are the indices of the inverse of the matrix representing g (Lee, 2012, p. 342), $\nabla f = g^{-1}\nabla_y f$ in T. Now

$$\int_M \sigma\langle\nabla v_i, \nabla v_j\rangle_g dS$$

$$= \sum_q \int_T \sigma(F_q(y))\langle\nabla v_i(F_q(y)), \nabla v_j(F_q(y))\rangle\sqrt{|g|}dy$$

$$= \sum_q \int_T \sigma(F_q(y))(\nabla_y v_i(F_q(y)))^T g^{-1}(\nabla_y v_j(F_q(y)))\sqrt{|g|}dy$$

since g (and g^{-1}) is symmetric.

Since $\partial M_{e_k} = \cup_{r,\beta} F_r(\partial_\beta T)$ for some $\mathcal{B}_k$, and since $F_r(\partial_\beta T)$ may only intersect at a single point, the boundary integrals in Lemma A3 can be mapped to the interval [0,1] by composing the appropriate F_r with one of the curves, $\gamma_1(t) = (t, 0)$, $\gamma_2(t) = (0, t)$, or $\gamma_3(t) = (t, 1-t)$, depending on which segments of $\partial_\beta T$ constitute to ∂M_{e_k} under F_r. On these boundaries, we may write $d\tilde{V} = \sqrt{|g_\omega|}dt$. Now, since the boundary integrals in Lemma A3 comprise only terms that correspond to an electrode e_k, and since these terms are zero if either a v_i or a v_j in the term is identically zero on ∂M_{e_k}, we are left with $\mathcal{I}$ as defined in the statement of the lemma. As an example

$$\sum_k^L \frac{1}{\zeta_k}\int_{\partial M_{e_k}} v_j v_i d\tilde{S}$$

$$= \sum_k^L \sum_{(q,\alpha)\in\mathcal{B}_k} \int_{\partial_\alpha T} \frac{U_k}{\zeta_k} v_j(F_q(\tilde{y}))v_i(F_q(\tilde{y}))\sqrt{g_\omega}d\tilde{y}$$

$$= \sum_k^L \sum_{(q,\alpha)\in\mathcal{B}_k} \int_0^1 \frac{U_k}{\zeta_k} v_j(F_q(\gamma_\alpha(t)))v_i(F_q(\gamma_\alpha(t)))\sqrt{g_\omega}dt$$

Now $\int_0^1 \frac{U_k}{\zeta_k} v_j(F_q(\gamma_\alpha(t)))v_i(F_q(\gamma_\alpha(t)))\sqrt{g_\omega}dt = 0$ if either $v_i(F_q(\gamma(t))) \equiv 0$ or $v_j(F_q(\gamma(t))) \equiv 0$, meaning that we can replace $(q,\alpha) \in \mathcal{B}_k$ with $(q,\alpha) \in \mathcal{I}(i,j,k)$. □

ALGORITHM 1 PDPS algorithm with two dual blocks

1: Choose step parameters $t, s_1, s_2 > 0$.
2: Choose initial iterates x^0, y_1^0, y_2^0.
3: **for all** $i \geq 0$ **until** a stopping criterion is satisfied **do**
4: $\quad x^{i+1} := \min\left\{\max\left\{\frac{t^{-1}(x^i - tK_1^T y_1^i - tK_2^T y_2^i) + \beta z^k}{t^{-1}+\beta}, \sigma_m\right\}, \sigma_M\right\}$
5: $\quad \bar{x}^{i+1} := 2x^{i+1} - x^i$
6: $\quad y_1^{i+1} := \frac{y_1^i + s_1(K_1^k \bar{x}^{i+1} - b^k)}{1+s_1}$
7: $\quad$ **if** total variation is used **then**
8: $\quad\quad y_2^{i+1} := \frac{y_2^i + s_2 K_2 \bar{x}^{i+1}}{\max\{\mathbf{1}, |y_2^i + s_2 K_2 \bar{x}^{i+1}|_2\}}$
9: $\quad$ **else**
10: $\quad\quad y_2^{i+1} := \frac{y_2^i + s_2 K_2 (\bar{x}^{i+1} - \sigma_{\text{ref}})}{1+s_2}$
11: $\quad$ **end if**
12: **end for**

ALGORITHM 2 RIPGN algorithm for problem (6). For the first cracking state, $\sigma^l = \sigma_{\text{ref}}$

1: Choose $\delta > 0$, $t > 0$ (for Algorithm 1), and $\beta > 0$.
2: $z^0 = \sigma^l$.
3: $s_2 := (1-\delta)/[2t\|K_2\|^2]$
4: **for all** $k \geq 0$ **until** a stopping criterion is satisfied **do**
5: $\quad$ Compute $I(z^k)$ by solving (4).
6: $\quad$ Compute $\nabla I(z^k)$.
7: $\quad K_1 := \mathcal{L}\nabla I(z^k)^T$
8: $\quad b^k = K_1^k z^k - \mathcal{L}(I(z^k) - I^M + \epsilon)$
9: $\quad s_1 := (1-\delta)/[2t\|K_1^k\|^2]$
10: $\quad$ Using Algorithm 1 with parameters t, s_1, s_2 and initial iterates $x^0 := z^k$, $y_1^0 := 0$, and $y_2^0 := 0$, find an approximate solution $\tilde{x}^k = x^i$ to (A11).
11: $\quad$ Find an optimal w using direct search.
12: $\quad z^{k+1} := z^k + w(\tilde{x}^k - z^k)$
13: **end for**
14: $\sigma^{l+1} = z^{k+1}$

The FE solver used in this work is part of the Julia code package developed for the nonplanar ERT by the authors (cf. Section 3.2). We note, however, that various computationally efficient alternatives for the FEM implementation exist. For example, in Yu and Adeli (1993) the FEM for stress analysis was implemented in C++ using object-oriented programming.

A.2 | Inversion algorithm

We now describe the RIPGN algorithm (Jauhiainen et al., 2020) specialized to our ERT problem (6). Presented in Algorithm 2, it utilizes the block-adapted PDPS of Valkonen (2019), presented in Algorithm 1, to solve the linearized inner problems of (6),

$$\arg\min \frac{1}{2}\|K_1^k x - b^k\|^2 + F(x) + \delta_V(x) + \frac{\beta}{2}\|x - z^k\|^2 \tag{A11}$$

where $K_1^k := \mathcal{L}\nabla I(z^k)^T$, $b^k = K_1^k z^k - \mathcal{L}(I(z^k) - I^M + \epsilon)$, and $x \in V$ is included in the problem through $\delta_V(x)$. After solving (4), the Jacobian of I, denoted $\nabla I(z^k)^T$, can be computed using the same approach as in planar geometry. This approach is described, for example, in Jauhiainen et al. (2020). Note that some parameters are fixed, since changing them is not necessary in ERT applications. For our numerical experiments in Sections 3 and 4, we use step length parameters $t = 10^{-5}$, $\delta = 10^{-3}$, and $\beta = 10^{-10}$; for further details and justifications of these choices, see Jauhiainen et al. (2020).

Algorithm 1 is derived from Jauhiainen et al. (2020, Algorithm 3.1) by expanding the so-called proximal operators in the latter. Specifically Line 4 is obtained by writing out $x^{i+1} := \text{prox}_{tG}(x^i - t(K_1^T y_1^i + K_2^T y_2^i))$, for $G(x) = \delta_V(x) + \frac{\beta}{2}\|x - z^k\|^2$, and Line 6 is obtained by writing out $y_1^{i+1} := \text{prox}_{s_1 F_1^*}(y_1^i + s_1 K_1 \bar{x}^{i+1})$ for $F_1(y) = \frac{1}{2}\|y - b^k\|^2$. Here G^* and F^* denote the convex conjugates of G and F.

Further, Line 8, which corresponds to the TV regularization (7), is obtained by writing out $y_2^{i+1} := \text{prox}_{s_2 F_2^*}(y_2^i + s_2 K_2 \bar{x}^{i+1})$ for $F_2(y) = \||y|_2\|_1$, where the operator $K_2 \in \mathbb{R}^{2N_e \times N_n}$ is the gradient operator. Here N_e denotes the number of elements and N_n denotes the number of nodes in the FE mesh. Note that $K_2 x$ has two components for each FE element. The norm $|\cdot|_2$ is the Euclidean length of these two components and $\|\cdot\|_1$ is a sum of these lengths (i.e., L_1 norm). Finally, Line 10, which corresponds to the smooth regularization function (8), is obtained by expanding $y_2^{i+1} := \text{prox}_{s_2 F_2^*}(y_2^i + s_2 K_2 \bar{x}^{i+1})$ with $F_2(y) = \frac{1}{2}\|y - K_2\sigma_{\text{ref}}\|^2$, where $K_2 = R_\Gamma \in \mathbb{R}^{N_n \times N_n}$.